The DOE E3SM Version 2.1: Overview and Assessment of the Impacts of Parameterized Ocean Submesoscales

Katherine M. Smith[1], Alice M. Barthel[1], LeAnn M. Conlon[1], Luke P. Van Roekel[1], Anthony Bartoletti[2], Jean-Christophe Golaz[2], Chengzhu Zhang[2], Carolyn Branecky Begeman[1], James J. Benedict[1], Gautam Bisht[3], Yan Feng[4], Walter Hannah[2], Bryce E. Harrop[3], Nicole Jeffery[1], Wuyin Lin[5], Po-Lun Ma[3], Mathew E. Maltrud[1], Mark R. Petersen[1], Balwinder Singh[3], Qi Tang[2], Teklu Tesfa[3], Jonathan D. Wolfe[1], Shaocheng Xie[2], Xue Zheng[2], Karthik Balaguru[3], Oluwayemi Garuba[3], Peter Gleckler[2], Aixue Hu[6], Jiwoo Lee[2], Ben Moore-Maley[1], and Ana C. Ordoñez[2]

[1]Los Alamos National Laboratory, Los Alamos, NM, USA
[2]Lawrence Livermore National Laboratory, Livermore, CA, USA
[3]Pacific Northwest National Laboratory, Richland, WA, USA
[4]Argonne National Laboratory, Lemont, IL, USA
[5]Berkeley Livermore National Laboratory, Berkeley, CA, USA
[6]National Center for Atmospheric Research, Boulder, CO, USA

Correspondence: Katherine M. Smith (kmsmith@lanl.gov)

Abstract. The U.S. Department of Energy's Energy Exascale Earth System Model (E3SM) version 2.1 builds on E3SMv2 with several changes, the most notable being the addition of the Fox-Kemper et al. (2011) mixed layer eddy parameterization. This parameterization captures the effect of finite-amplitude, mixed layer eddies as an overturning streamfunction and has the primary function of restratification. Herein, we outline the changes to the mean climate state of E3SM that were introduced by the addition of this parameterization. Overall, the presence of the submesoscale parameterization improves the fidelity of the v2.1 simulation by reducing the North Atlantic ocean surface biases present in v2, as illustrated by changes to the climatological sea surface temperature and salinity, as well as Arctic sea-ice extent. Other impacts include a slight shoaling of the mixed layer depths in the North Atlantic, as well as a small improvement to the Atlantic Meridional Overturning Circulation (AMOC). We note that the expected shoaling due to the parameterization is regionally dependent in our coupled configuration. In addition, we investigate why the parameterization and its impacts on mixed layer depth have little impact on the simulated AMOC: despite increased dense water formation in the Norwegian Sea, only a small fraction of the water formed makes its way south into the North Atlantic basin. Version 2.1 also exhibits small improvements in the atmospheric climatology, with smaller biases in many notable quantities and modes of variability.

1 Introduction

The U.S. Department of Energy (DOE) Energy Exascale Earth System Model (E3SM) aims to meet the energy mission and science needs of the DOE using state-of-the-art DOE computing resources. Version 1 (E3SMv1) was released in 2018 and, while the land model and coupler were similar to those in CESM2 (Community Earth System Model, Hurrell et al. (2013); Dan-

abasoglu et al. (2020)), the river routing, ocean, sea ice, atmospheric physics, atmospheric dynamical core, and stratospheric chemistry were significantly different. Both lower (110 km atmosphere and 60-30 km ocean) and higher (25 km atmosphere and 18-6 km ocean) resolution configurations were released (Golaz et al., 2019; Caldwell et al., 2019), along with biogeochemical and cryosphere configurations (Burrows et al., 2020; Comeau et al., 2022). Following version 1, version 2 (E3SMv2) was released in 2022 with significant improvements to the modeled climate, including a 2x speedup from E3SMv1 (Golaz et al., 2022). For this version, a lower resolution configuration and a North American regionally refined configuration (Tang et al., 2023) have been released, with plans for a biogeochemistry configuration with interactive carbon and nutrient cycles, and a cryosphere configuration with regional refinement over the Southern Ocean in the future.

Version 2.1 (E3SMv2.1) builds on E3SMv2 (Golaz et al., 2022) with several changes, most notably the addition of the so-called "Fox-Kemper2011" mixed layer eddy (MLE) parameterization (hereafter referred to as FK11; Fox-Kemper et al. (2008); Fox-Kemper et al. (2011)). Shallow, ageostrophic baroclinic instabilities, often referred to as submesoscale instabilities, develop on lateral density fronts in the weakly stratified surface mixed layer. Once they become finite amplitude, the resulting mixed-layer eddies slump the fronts, releasing potential energy and contributing to the restratification and shoaling of the mixed layer (Boccaletti et al., 2007). Due to their small spatial scales ($\mathcal{O}(10\text{km})$), these submesoscale instabilities and their effects are not explicitly resolved in global ocean models, even at "eddy-resolving" resolutions, and thus need to be parameterized. Fox-Kemper et al. (2008) proposed a parameterization in the form of an overturning streamfunction to mimic the MLE fluxes of density and other tracers. By construction, this overturning streamfunction acts to slump isopycnals and enhance restratification of the mixed layer. This parameterization has been implemented in several other global ocean general circulation models, such as the Parallel Ocean Program (POP) model (Smith et al., 2010), the Modular Ocean Model (MOM) (Griffies, 2009; Adcroft et al., 2019), the Generalized Ocean Layered (GOLD) model (Adcroft and Hallberg, 2006), and the MIT General Circulation Model (MITgcm) (Marshall et al., 1997). According to Fox-Kemper et al. (2011), the general impacts of the parameterization within these models are the shoaling of the mixed layer (with greatest effects in polar winter regions), a strengthening of the Atlantic Meridional Overturning Circulation (AMOC), a reduction in tracer ventilation, small changes to sea surface temperature (SST) and air-sea fluxes, and a reduction in sea-ice basal melting.

In this paper, we largely focus on documenting the implementation of the MLE parameterization from FK11 in the ocean component of the E3SM, the Model for Prediction Across Scales - Ocean (MPAS-Ocean). We investigate the response of the coupled model to the MLE fluxes, with a particular focus on high-latitude convection and large-scale ocean circulation, including the AMOC.

2 Methods

E3SMv2.1 implemented several changes from v2, including several bug fixes and additional options that are detailed in Appendix B. However, the primary notable difference from E3SMv2 is the inclusion of the FK11 MLE parameterization, outlined below (Fox-Kemper et al., 2011). All other features listed in Appendix B are not active in the v2.1 configuration simulations used in this study, and any bug fixes were shown to have no significant climate changing effects in testing, thus we will assume

any changes from v2 to v2.1 are due to the addition of the FK11 MLE parameterization and any feedbacks it may induce in the model.

2.1 Mixed Layer Eddy Parameterization

The FK11 MLE parameterization captures finite-amplitude, mixed layer eddies as an overturning streamfunction and has the primary function of restratification. It applies a submesoscale transport velocity through a streamfunction given as

$$\Psi = C_e \frac{\Delta_S}{L_f} \frac{H^2 \nabla \overline{b}^z \times \hat{\mathbf{z}}}{\sqrt{f^2 + \tau^{-2}}} \mu(z), \tag{1}$$

$$\mu(z) = \max \left\{ 0, \left[1 - \left(\frac{2z}{H} + 1 \right)^2 \right] \left[1 + \frac{5}{21} \left(\frac{2z}{H} + 1 \right)^2 \right] \right\}, \tag{2}$$

$$L_f = \max \left(L_{f,min}, \left| \nabla_H \overline{b}^z \right| H/f^2, NH/|f| \right), \tag{3}$$

where C_e is an efficiency coefficient, Δ_S is the local model grid-scale dimension, H is the mixed layer depth, $\overline{b}^z$ is the depth-average buoyancy over the mixed layer, $\hat{\mathbf{z}}$ is the unit vertical vector, f is the Coriolis parameter, τ is the time needed to mix momentum across the mixed layer, $L_{f,min}$ is a limiting value of L_f to guarantee stability (typically 0.2-5 km), and N is the buoyancy frequency. Eq. 1 can be physically interpreted as an overturning streamfunction that produces a bolus velocity ($u_{MLE} = \nabla \times \Psi$) that acts to slump fronts and provide MLE fluxes to tracers, Eq. 2 as a structure function for the vertical fluxes that has a maximum in the middle of the mixed layer and vanishes to zero at the surface and beneath the mixed layer, and Eq. 3 as an estimate of the typical local width of mixed layer fronts, set here in this model configuration as the mixed layer deformation radius. While recent work has been done to improve the representation of L_f (Bodner et al., 2023), we use the original formulation from Fox-Kemper et al. (2011) here in this study.

2.2 Model Setup

In order to test the impact of the above changes, we will compare simulations from the E3SMv2 (Golaz et al., 2022) and E3SMv2.1 configurations. As with E3SMv1 and v2, we will focus on climate metrics within the standard resolution configuration, which consists of a 110 km atmosphere, a 165 km land, 0.5° river routing model, and a variable resolution ocean and sea ice mesh going from 60 km in the mid-latitudes to 30 km at the equator and poles. Similarly, the vertical grid remains the same as E3SMv1 and v2, with 72 layers in the atmosphere (∼60 km top) and 60 layers in the ocean (10 m near-surface resolution). Just like v2, the ocean model uses the Gent-McWilliams (GM; Gent and Mcwilliams, 1990) and Redi parameterizations (Redi, 1982), to simulate mesoscale eddies, in addition to the MLE parameterization outlined above.

2.3 Simulations

Table 1 summarizes the v2 and v2.1 simulations used in this paper. The full Diagnosis, Evaluation and Characterization of Klima (DECK; Eyring et al. (2016)), five historical simulations, and two idealized CO_2 simulations were run for each configuration. In addition, for the purpose of this paper and investigation into the mechanisms of change due to the FK11 MLE

Table 1. Summary of E3SMv2 and E3SMv2.1 Simulations

Label	Description	Period	Ens.	Initialization
v2 piControl	Pre-Industrial control with v2 code base	500 yr	-	Pre-industrial v2 spin-up
v2 historical_N	Historical period with v2 code base	1850-2014	5	*v2 piControl* (yrs 101, 151, 201, 251, 301)
v2 piControl Ext	33-year piControl extension with v2 code base	501-533	-	*v2 piControl* (yr 500)
v2 1pctCO2	Prescribed 1% yr^{-1} CO_2 increase	150 yr	1	*v2 piControl* (101)
v2 abrupt-4xCO2	Abrupt CO_2 quadrupling	150 yr	1	*v2 piControl* (101)
v2.1 piControl	Pre-Industrial control with v2.1 code base	500 yr	-	Pre-industrial v2.1 spin-up
v2.1 historical_N	Historical period with v2.1 code base	1850-2014	5	*v2.1 piControl* (yrs 101, 151, 201, 251, 301)
v2.1 piControl Ext	33-year piControl extension with v2.1 code base	501-533	-	*v2.1 piControl* (yr 500)
v2.1 1pctCO2	Prescribed 1% yr^{-1} CO_2 increase	150 yr	1	*v2.1 piControl* (101)
v2.1 abrupt-4xCO2	Abrupt CO_2 quadrupling	150 yr	1	*v2.1 piControl* (101)

80 parameterization, we ran an additional 33-year extension on both the v2 and v2.1 *piControl* simulations that included several passive tracers (details provided below in Section 4). Historical ensemble members (*v2/v2.1 historical_N*) and the extension runs (*v2/v2.1 piControl Ext*) were initialized from the *v2/v2.1 piControl* on Jan 1 of the year indicated in Table 1. Both the v2 and v2.1 simulations were completed on the DOE-E3SM owned "Chrysalis" machine, which is a traditional high performance computer with 528 nodes with two AMD Epyc 7532 processors per node (64 cores per node) located at Argonne National Lab-

85 oratory. Computational performance between the two configurations is comparable, with v2 and v2.1 producing 42 simulated years per day and 40.5 simulated years per day on average, respectively, on 105 nodes of Chrysalis.

3 Overview of v2.1 Climate

In this section, we examine the climatological state of the v2.1 configuration. In particular, we focus on changes to the mean climate state that were introduced by the addition of the ocean MLE parameterization on the North Atlantic. For that purpose, we highlight the biases (with respect to observational estimates) in the context of the historical biases that were present in the v2 configuration.

3.1 Oceanic Climate

For a global evaluation of relevant oceanic fields and a comparison between the v2 and v2.1 configurations, we first present spatio-temporal correlations (CORR) and root mean squared error (RMSE) relative to observations in Figure 1. Annual ocean climatologies, correlations, and RMSE are constructed using the five member *v2/v2.1 historical* ensemble means over a 1980-2014 period. Observational data are drawn from merged Hadley Center-NOAA/OI data from 1870-2008 for the sea-surface temperature (SST) (Hurrell et al., 2008), from the NASA Aquarius satellite from 2011-2015 for sea-surface salinity (SSS) (Lagerloef et al., 2015), from merged absolute dynamic topography satellite data provided by AVISO (Archiving, Validation and Interpretation of Satellite Oceanographic data; processed by SSALTO/DUACS and distributed by AVISO+ (https://www.aviso.altimetry.fr) with support from CNES) from 1992-2010 for sea-surface height (SSH), from ARGO floats and the NCEI-NOASS World Ocean Database (WOD; Boyer et al. (2018)) through the SEANOE data product from 1970-2021 for the mixed layer depth (MLD) (de Boyer Montégut et al., 2004), and Global Drifter Program drifters from 1979-2015 for near-surface eddy kinetic energy (EKE) (Laurindo et al., 2017).

Correlations serve to evaluate the model's ability to represent spatial patterns, while RMSE evaluate the model's representation of magnitude (although spatial patterns are also represented in RMSE), in comparison to observations. While modest, all correlation quantities increase across all ensemble members from the v2 to v2.1 configuration, indicating a better model representation of spatial patterns due to the presence of the MLE parameterization. For RMSE, although they are relatively modest, SST, SSS, and EKE see a small global bias reduction going from the v2 to v2.1 configuration, and this reduction is seen across all ensemble members. While the mean MLD RMSE for the v2.1 configuration is slightly less than the v2 configuration, the ensemble spreads are essentially overlapping, indicating little difference between the two. Climatological maps of MLD biases discussed later in Figure 5 indicate that the MLDs have changes in regional biases, where some regions see improvements and some degradation going from the v2 to v2.1 configuration, that compensate for each other when looking at this global RMSE metric.

There is an increase in the global SSH RMSE, which can be attributed to an initial ∼1.5-2 cm global increase in the first few years of the v2 *piControl* simulation that is not present in the v2.1 *piControl* simulation. This ∼1.5-2 cm offset remains throughout the v2 *piControl* and each *historical* ensemble simulation. Plotting maps of global *v2/v2.1 historical* climatological SSH (not shown) reveal this step decrease to be globally uniform going from the v2 vs v2.1 configuration, and time series comparing SSH anomalies from v2 and v2.1 shown in Figure 2 show the global anomaly ensemble spreads for the two different model versions to be essentially overlapping throughout the *historical* simulations and having a similar trend over time to

 observations. Taking this into account and the increased correlation metric for SSH (indicating better model SSH gradients), we believe overall the v2.1 configuration does not exhibit a degraded global climatological SSH in comparison to the v2 configuration. In order to understand regionally where each of the bias changes for MLD, SST, and SSS occur, we next dive into a series of ocean climatological maps.
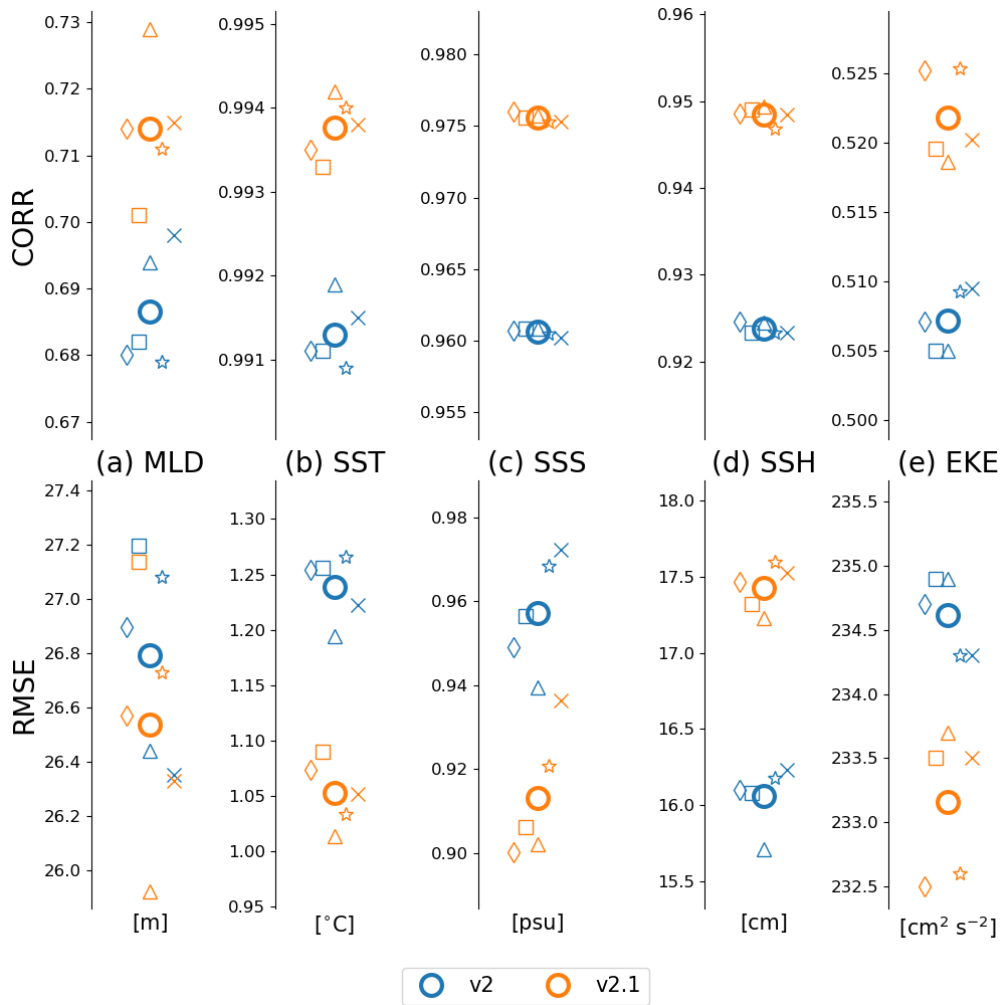
Figure 1. Correlations (top row) and RMSE (bottom row) of the global MLD (m), SST (°C), SSS (psu), SSH (cm), and EKE (kg^2 s^{-2}) for the v2 (blue markers) and v2.1 (orange markers) *historical* ensemble simulations relative to observations (see text for data citations). Different symbols indicate the metric obtained from individual ensemble members and thick, open circle markers indicate the multi-realization averages of the five *v2/v2.1 historical* ensemble members over a 1980-2014 time period. Individual ensemble members have been spread out on the x-axis to help with visualization of overlapping values.
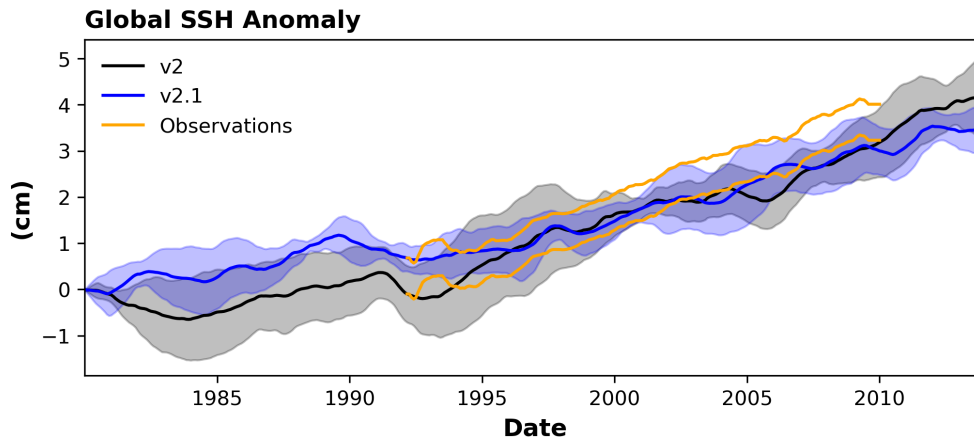
Figure 2. Time series of global SSH anomaly for the v2 (black) and v2.1 configuration (blue), and observations (orange). Thick lines denote the mean, while shading illustrates one standard deviation from that mean.

In the following, we present a series of ocean climatological maps where panel (a) is the v2 configuration bias in comparison to observations, panel (b) is the v2.1 configuration bias in comparison to observations, and panel (c) is the change in biases between the v2.1 and v2 configurations (ie. positive (negative) values are an increase (decrease) in bias in the v2.1 quantity compared to v2). In these fields, we mask out values considered not statistically significant according to a one-sample T-test (and a two-tailed critical value at alpha = 0.05) when comparing the model ensemble to observations, and a two-sample T-test when comparing the two model ensembles. Since most of the significant oceanic changes from v2 to v2.1 are within the North Atlantic and Arctic Oceans, the figures here focus on those regions. Figures of the full global ocean climatological biases are provided in Appendix A. Observational data are the same products used in the RMSE and correlation calculations of Figure 1.

In general, the presence of the MLE parameterization improves the fidelity of the v2.1 configuration by reducing the North Atlantic Ocean surface biases present in v2 (Golaz et al., 2022), as illustrated by changes to the climatological sea-surface temperature (SST; Figure 3) and sea-surface salinity (SSS; Figure 4). A reduction in the v2 sea-ice biases is also seen and is discussed in Section 3.4.

Looking in more detail at the SST field, Figure 3 shows that although the *v2.1 historical* simulation ensemble retains large-scale SST biases (Figure 3b) qualitatively similar to that of the v2 simulations (Figure 3a) – namely a meridional dipole of excess heat in the South Atlantic and a cold bias in the North Atlantic – v2.1 presents a significant SST bias reduction (blue shading in Figure 3c), focused primarily on the North Atlantic subpolar gyre, the Nordic Seas and Southern Ocean (see Appendix A, Figures A1, A2, and A3), reducing the temperature bias by 0.5-2°C. Differences for all regions, including the Southern Ocean, can be found in Appendix A.
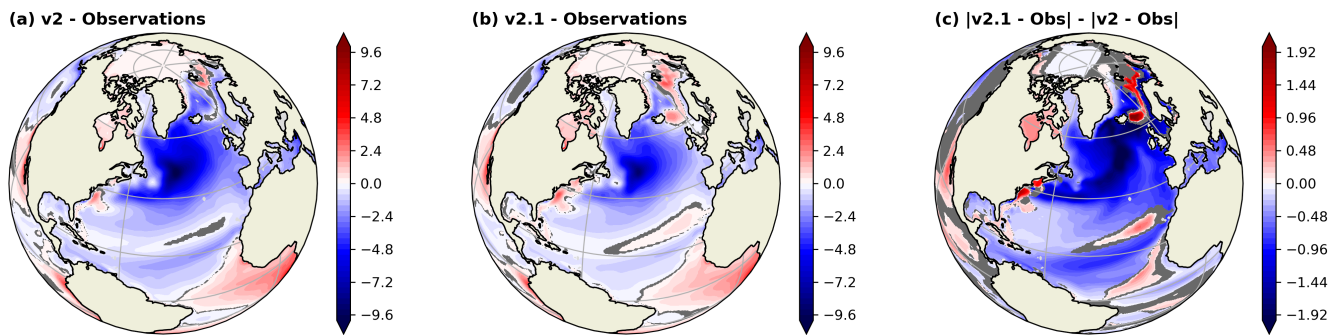
Figure 3. Annual climatological SST biases (°C) with respect to observations for the (a) v2 and (b) v2.1 configurations. (c) Change in SST biases between v2.1 and v2 configurations. Regions shaded in light gray denote where there is no data and regions shaded in dark gray denote where the difference is not significant (according to a one-sample T-test in (a,b) and a two-sample T-test in (c)).

Likewise, *v2.1 historical* simulation ensemble shows an improvement in the SSS bias in the North Atlantic, as shown by the blue region in Figure 4c. The addition of the submesoscale parameterization is insufficient to fully mitigate the large scale cold, fresh bias in the North Atlantic (still visible in blue in Figures 3b and 4b), but leads to an improvement of 0.5-1 psu in the North Atlantic including both the subtropical and subpolar gyres, as well as the Nordic Seas. In the Barents, Kara, and Laptev seas, the bias reduction is even higher (1-2 psu). The v2.1 configuration and the presence of the MLE parameterization, however, do not appear to help the persistent salty SSS biases in the deep tropical North Atlantic, Beaufort and Chukchi Seas, and Indian Ocean (see Appendix A).
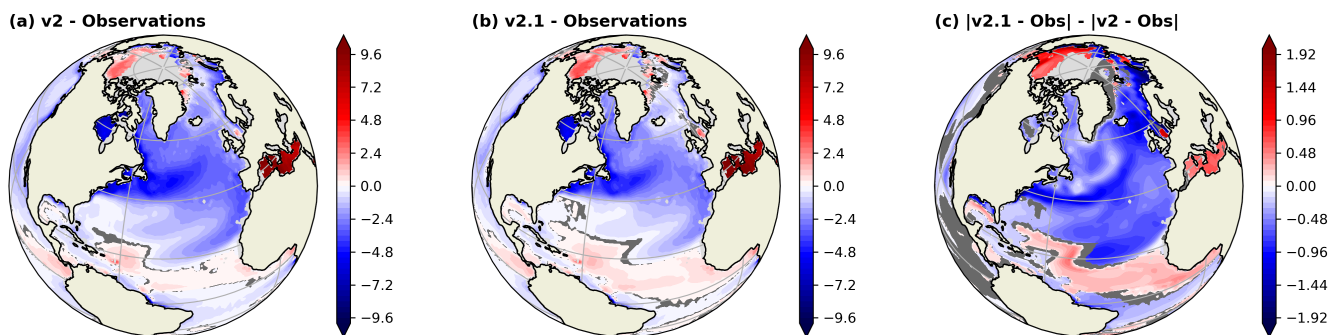
Figure 4. Same as Figure 3 but for SSS (psu).

Mixed layer depths (MLD) do not show the same North Atlantic bias reduction as SST and SSS. In particular, the *v2.1*

150 *historical* simulation ensemble resulted in a slight shoaling of the mixed layer of approximately 20 meters, increasing the bias over much of the North Atlantic (Figure 5). This is most pronounced within the subpolar gyre, Nordic Seas, and eastern North Atlantic (red shading in Figure 5c). This shoaling of the MLD is one of the primary effect of the FK11 MLE parameterization (Fox-Kemper et al., 2011)). A localized decrease in MLD does occur in the vicinity of the Gulf Stream as the v2 deep biases there are significantly reduced.
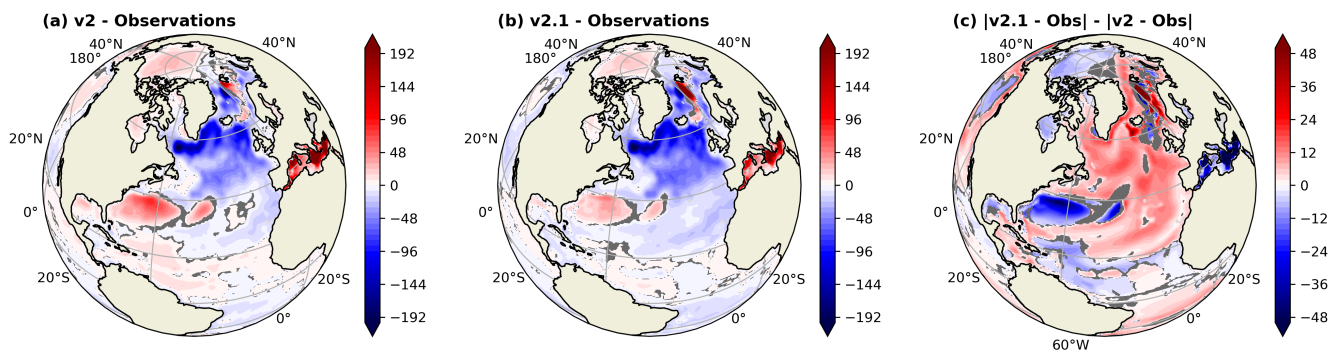
Figure 5. Same as Figure 3 but for MLD (m).

155   A small uptick in the strength of the AMOC is seen (Figure 6), as well as a reduction in the variability (a noted effect of the FK11 MLE parameterization (Fox-Kemper et al., 2011)). However, a larger increase in strength was expected given the reductions in the SST and SSS biases, which are likely responsible in part for reduced deep water formation in the North Atlantic that should feed into the AMOC. We explore reasons for this difference in expected versus actual outcomes in Section 4. The bias differences in SSH or EKE are relatively small and not regionally focused, but rather somewhat uniform across the global

160   oceans, and are therefore not shown here.
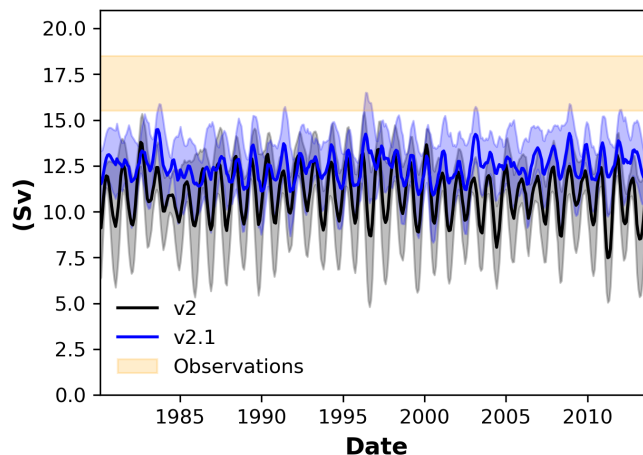
Figure 6. Time series of the maximum AMOC (Sv) at 26.5 N for the E3SM v2 configuration (black), the E3SM v2.1 configuration (blue), and an estimate of the observational range (orange) over the 1980-2014 period. Thick lines denote the ensemble mean, while shading illustrates one standard deviation from that mean, after a 12-month smoothing is applied.

3.2 Atmospheric Climate

For a collective evaluation of atmospheric fields and comparison of their performance between E3SMv2 and v2.1, we applied the Program for Climate Model Diagnosis and Intercomparison (PCMDI) Metrics Package (PMP; Lee et al., 2024), which is an open-source Python software package that provides quick-look objective comparisons of ESMs with one another and with observations. In Figure 7, model performances in reproducing observed global climatologies of multiple surface and upper-air fields are assessed, which include precipitation, sea level pressure, radiation at the surface and top of atmosphere, air temperature at 200 and 850 hPa, surface air temperature, surface temperature, and wind components at 200 and 850 hPa and 500 hPa geopotential height. The spatio-temporal RMSE (Gleckler et al., 2008) was calculated, which is derived by getting a spatial RMSE of each calendar month of climatological annual cycle and then averaging it across months. Although the differences are small, Figure 7 indicates most fields in v2.1 have a reduced bias compared to v2. The improvement in surface temperature ("ts") and near-surface air temperature ("tas") is noticeable, which may be dominated by the improvement of the sea-surface temperature field as shown in Figure 3.
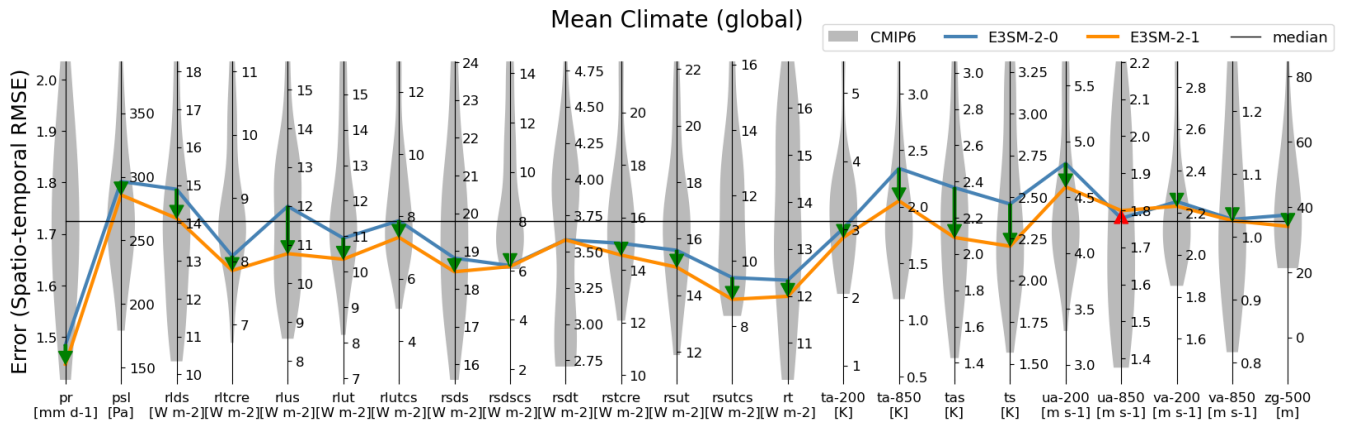
Figure 7. The PMP Parallel Coordinate Plot (Lee et al., 2024) for global mean climate evaluation, showing the spatio-temporal RMSE (Gleckler et al., 2008). Each vertical axis represents a different variable. Full names for model variables on the abscissa and their reference datasets can be found in Table 1 of Lee et al. (2024). RMSEs are constructed using the five *v2/v2.1 historical* ensemble member over a 1981-2005 time period. Improvement (degradation) in E3SM v2.1 compared to E3SM v2 is highlighted as a downward green (upward red) arrow between lines. The midpoint of each vertical axis is shifted to represent the median result from the CMIP6 multi-model ensemble (horizontal black line), with the axis range stretched to the minimum and maximum from the median CMIP6 for visual consistency. The inter-model distributions of CMIP6 model performance are shown as shaded violin plots along each vertical axis. First historical ensemble member of each model is used for the assessment.

3.3 Extratropical Modes of Variability

To examine the influence of the model update to the interannual climate variability modes, we applied the PMP's metrics for
extratropical modes of variability (ETMoVs) for E3SMv2.1 and v2. Specifically, we have evaluated five atmospheric-based
ETMoVs including the Northern Annular Mode (NAM), North Atlantic Oscillation (NAO), Pacific North America pattern
(PNA), North Pacific Oscillation (NPO), and Southern Annular Mode (SAM), as well as two based on sea-surface temperature
(SST): the Pacific Decadal Oscillation (PDO), and North Pacific Gyre Oscillation (NPGO). The atmospheric ETMoVs were
evaluated for four seasons, while monthly time series were directly used for the SST-based modes. The Common Basis Function
(CBF) approach is used to ensure a fair comparison of ETMoVs as simulated by climate models (Lee et al., 2019, 2021, 2024).
The metric we selected for this study is the spatio-temporal RMSE obtained from the comparison of the model's CBF pattern to
the observed empirical orthogonal functions (EOF) pattern, which enables the inter-model comparison of bias magnitude that
is from both the pattern and amplitude (Lee et al., 2019). To gauge the influence of internal variability in the evaluation process,
we use the five *v2/v2.1 historical* ensemble members. Metrics were calculated for each ensemble member of the model, then
averaged across the five realizations. In Figure 8, there are 14 metrics that show improvement including NAM and NAO and
8 cases of degradation. The ETMoV performance has not substantially changed in the context of the inter-model spread of
CMIP6 models (shown as gray violin plots in the background). In summary, the large-scale extratropical modes of variability
are not substantially different between E3SMv2 from v2.1.
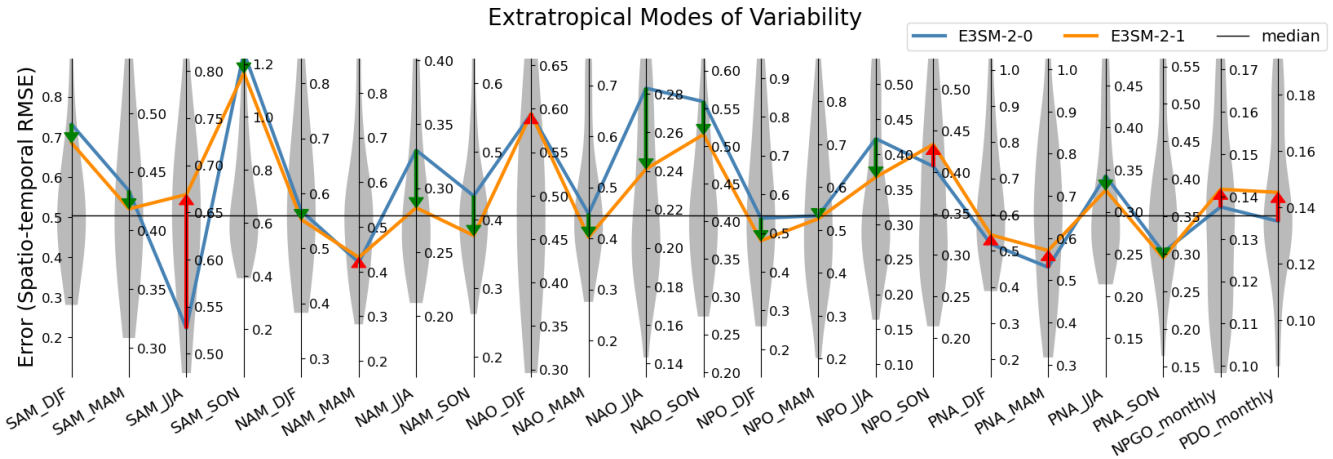
Figure 8. The PMP Parallel Coordinate Plot (Lee et al., 2024) for extratropical modes of variability evaluation, showing the spatio-temporal
RMSE (Lee et al., 2019). Each vertical axis represents a different mode and season. Analysis is constructed using the five *v2/v2.1 histori-
cal* ensemble members over a 1900-2005 time period. Improvement (degradation) in E3SMv2.1 compared to E3SMv2 is highlighted as a
downward green (upward red) arrow between lines. Similar to Figures 7, the middle of each vertical axis is set to the median of the group of
benchmarking models (i.e., CMIP6), with the axis range stretched to maximum distance to either minimum or maximum from the median
for visual consistency. The inter-model distributions of model performance are shown as shaded violin plots along each vertical axis.

3.4 Sea-Ice Climate

190 Similar to Section 3.1, in Figures 9 and 10 we plot climatological means of sea ice properties constructed using the five member *v2/v2.1 historical* ensemble means over a 1980-2014 period. Observational data are derived using measurements from multiple sensors across many satellite platforms detailed in Comiso (2017). Figure 9 shows an improvement in v2.1 Arctic sea-ice concentration, particularly around the Nordic Seas, Greenland, and the Labrador Sea (blue shading in Figure 9c). Figure 10 shows a mix of improvement in the Indian Ocean and degradation in the Weddell, Amundsen, and Ross Seas for v2.1 Antarctic

195 sea-ice concentration.
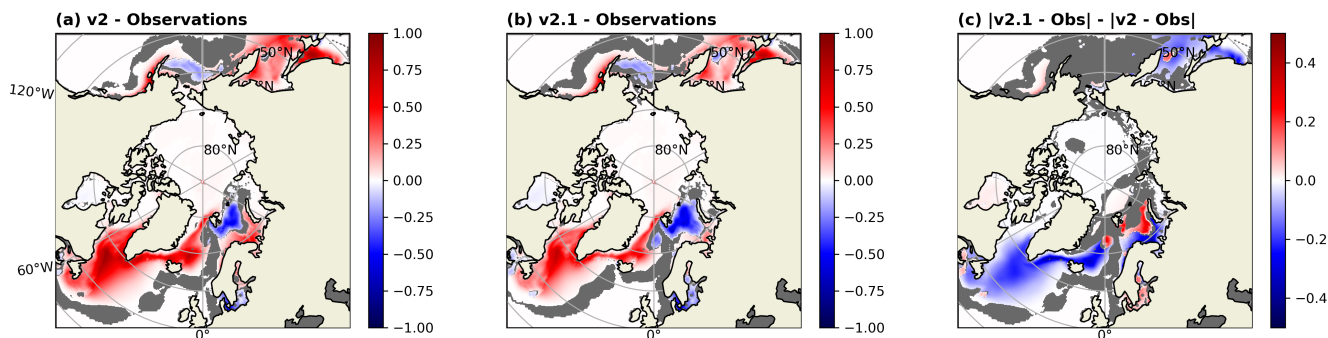
Figure 9. Annual climatological sea-ice concentration (fraction) biases with respect to observations in the Arctic for the (a) v2 and (b) v2.1 configurations. (c) Change in sea-ice concentration biases between v2.1 and v2 configurations. Regions shaded in dark gray denote where the difference is not significant (according to a one-sample T-test in (a,b) and a two-sample T-test in (c)).
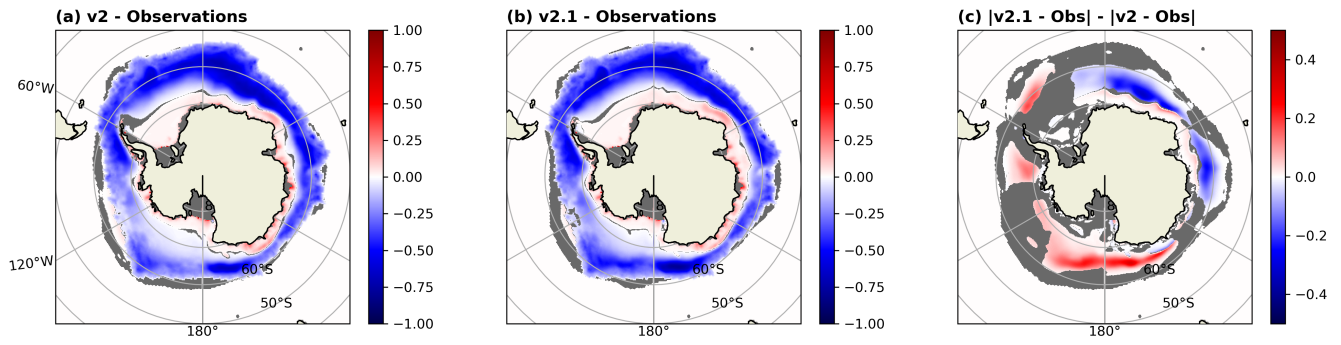
Figure 10. Same as Figure 9 but for the Antarctic.

We evaluated the time mean and climatological annual cycle of sea-ice area in both the Arctic and Antarctic. In the calculation of the metric, we defined sea-ice area following Ivanova et al. (2016) as the area of grid cells with greater than 15% sea ice coverage (i.e. 15% ice concentration) multiplied by their fraction of coverage and summed across grid cells within each region. For each of the Arctic and Antarctic regions, we partitioned the geographical region into three domains following Ivanova et al. (2016). The Arctic region is separated into the North Pacific, Central Arctic, and North Atlantic (shown in Figure A5 in Appendix A), and the Antarctic region is separated to the South Atlantic, Indian Ocean, and South Pacific domains (shown in Figure A6 in Appendix A). The model output is evaluated against the EUMETSAT OSI-SAF satellite based product (Ocean and Facility, 2022). A date range of 1988-2014 was chosen for the maximal overlap between the *v2/v2.1 historical* simulations and periods without missing data in the OSI-SAF product. The sea-ice area metrics that were proposed by Ivanova et al. (2016) and recently implemented in the PMP (Lee et al., 2024) are used for the analysis. We derived a simulated annual cycle and annual mean of the sea-ice area in each region for the time period of 1988-2014, to compare with observations (Figure 11). The evaluation metrics are defined as mean square errors in the the climatological annual cycle after removing the annual mean, and annual mean of the sea ice area (Figure 12). The overestimation of sea-ice area over the North Atlantic, North Pacific (mostly in December to May, Figure 11) and the Central Arctic (in August to September, Figure 11), and the underestimation over the Indian Ocean (in July to October, Figure 11) sub-regions in v2 are noticeably alleviated in v2.1, while the changes in other regions do not appear to be substantially different.
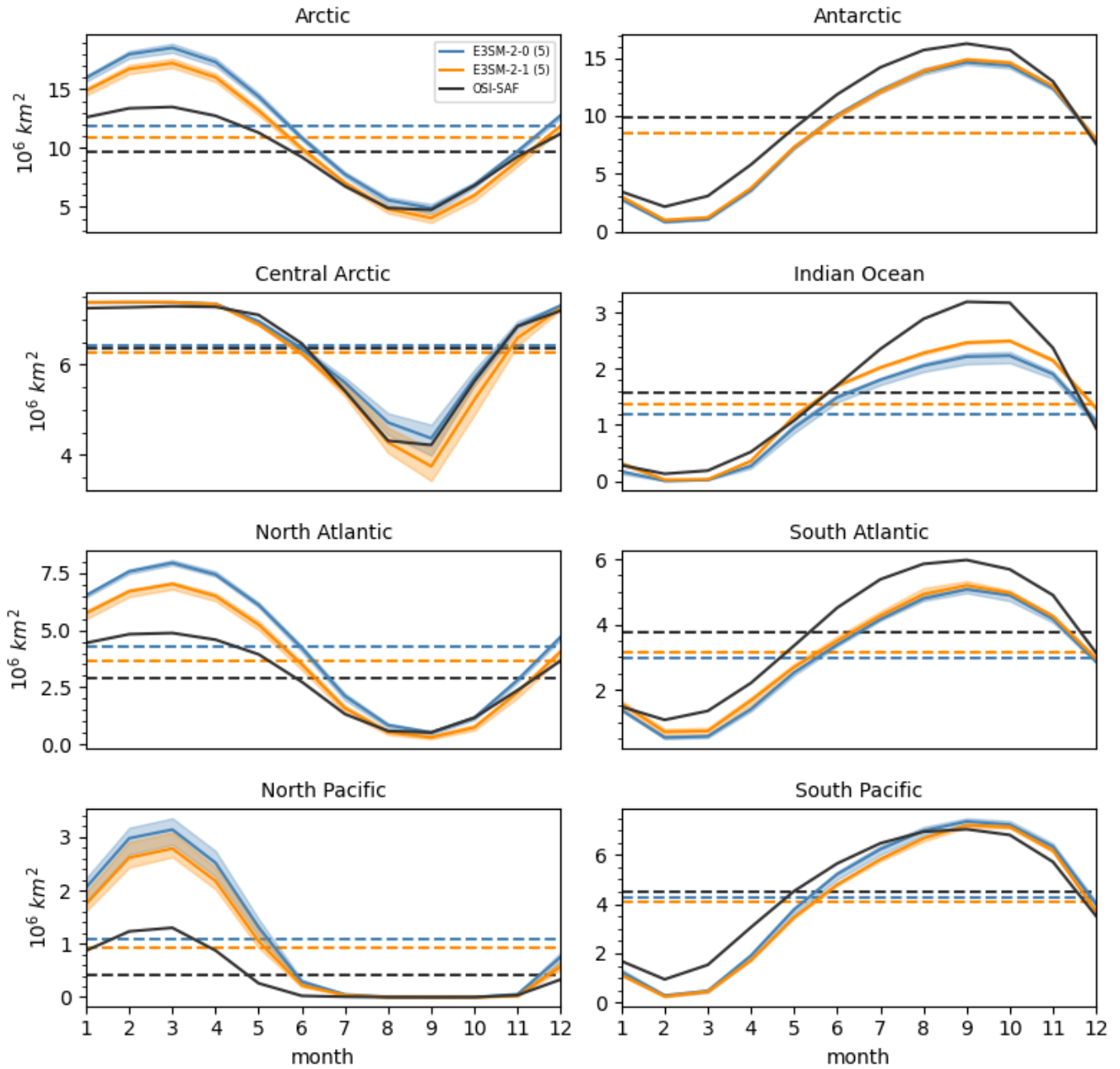
Figure 11. Climatological annual cycle (1988-2014) of total sea-ice area in the entire Arctic and its sub-regions (left) and the entire Antarctic and its sub-regions (right), obtained from the E3SMv2 (blue) and v2.1 (orange) simulations, and the reference dataset EUMETSAT OSI-SAF (black line). Solid lines indicate the average of the five ensemble members while the shaded color indicates inter-ensemble spread. Dashed horizontal lines indicate the respective annual mean of the sea-ice area. In Antarctic panel, the blue dashed line is hidden beneath the orange dashed line.
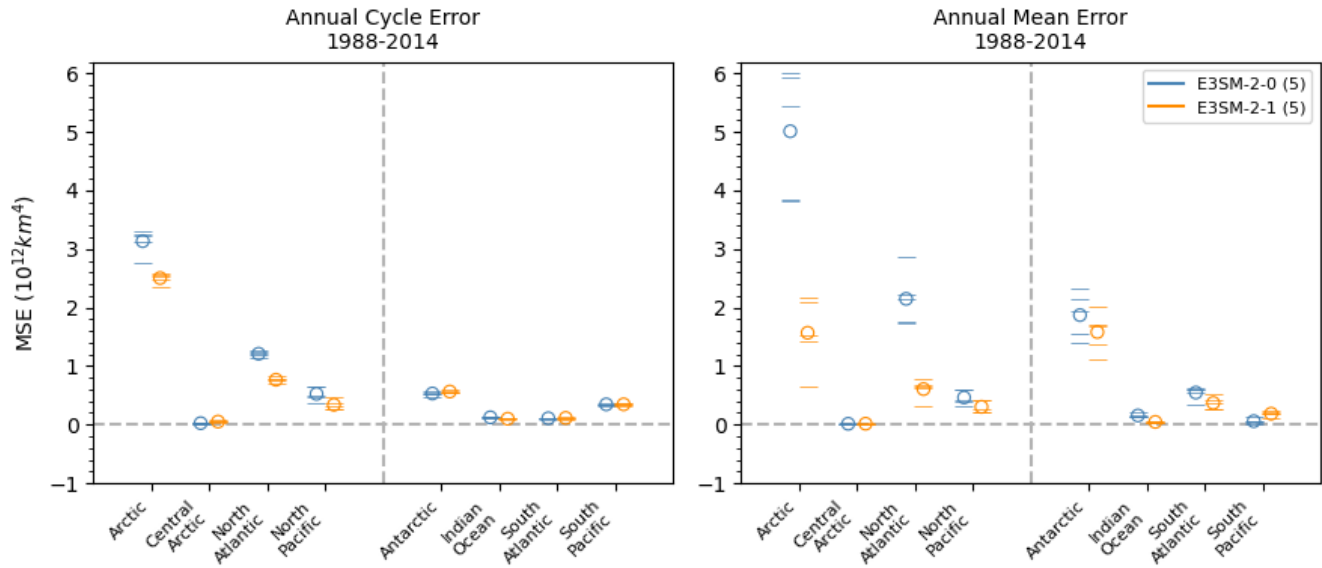
Figure 12. Mean square error (MSE) of the total sea-ice area annual cycle (annual mean removed; left) and annual mean (i.e., time-mean bias squared; right) of each Arctic and Antarctic sub-region. Horizontal line markers indicate the metric obtained from individual ensemble members and open circle markers indicate the multi-realization averages of the five ensemble members for each sub-region. Lower values are better. The gray vertical dashed line separates sub-regions of Arctic (left) and Antarctic (right) in each panel. The diagnosed annual means and cycles for all regions, simulations, and the reference dataset can be found in Figure 11.

3.5 Climate Sensitivity and Transient Climate Response

We also performed two idealized CO_2 simulations (*v2/v2.1 1pctCO2* and *v2/v2.1 abrupt-4xCO2*) to estimate the model sensitivity to CO_2-forcing at different time scales. The equilibrium climate sensitivity (ECS) is defined as the equilibrium surface temperature change resulting from a doubling in CO_2 concentrations. ECS is typically approximated by linear regression of top-of-atmosphere radiation vs. surface temperature in a 150 yr "abrupt-4xCO2" simulation (Gregory et al., 2004), often referred to as "effective climate sensitivity". Response on shorter time scales is measured by the transient climate response (TCR) defined as the change in surface temperature averaged for a 20 year period around the time of CO_2 doubling from a "1pctCO2" simulation. TCR depends on both climate sensitivity and ocean heat uptake rate.

ECS is nearly unchanged in E3SMv2.1 at 3.92 K compared to 4.0 K in E3SMv2. TCR is slightly smaller at 2.20 K compared to 2.41 K. Both values are substantially smaller than E3SMv1 which suffered from a high sensitivity (ECS of 5.30 K and TCR of 2.93 K; Golaz et al., 2019). Meehl et al. (2020) evaluated ECS and TCR for 37 CMIP6 models. They found that the multimodel mean ECS was 3.7 ± 1.1 K (standard deviation). The multimodel mean TCR was 2.0 ± 0.4 K. E3SMv2.1 is well within one standard deviation of multimodel mean for both ECS and TCR, but higher than the mean.

In the next section, we delve into the potential mechanisms for the changes in biases present in the North Atlantic Ocean, as well as potential links between those biases and AMOC.

4 Relationship between AMOC and North Atlantic state

In order to shed light on mechanisms creating these changes, in particular the relationship between AMOC and the North Atlantic biases, we examined several variables in detail. This was done in an effort to relate deep water formation and overturning to surface biases. To do this, we primarily investigated tracer transports through the North Atlantic via a 33-year *piControl* extension run for both the v2 and v2.1 configurations (*v2/v2.1 piControl Ext*), with three additional passive tracers. At year 501 of both the v2 and v2.1 *piControl* simulations, we added three passive tracers and ran the simulations out to year 533. The injection of one tracer was proportional to the sea-ice fresh water flux into/out of the ocean, the second was set to one in the first grid layer globally at every time step, and the last was set to one in the first grid layer at every time step, but only within a North Atlantic latitude and longitudinal band of $50° - 80°$N and $60°$W$-10°$E, respectively. Conclusions from each of these tracers were roughly the same, so for clarity we only show and discuss the third tracer. For consistency between plots and analysis in this section, all figures and analysis utilize these *v2/v2.1 piControl Ext* runs with passive tracers, instead of the ensemble *v2/v2.1 historical* runs utilized in the previous sections.

Figure 13 shows the annual climatological (a-b) MLD and (d-e) sea-ice concentration in the Nordic seas for the (a,d) v2 and (b,e) v2.1 configurations, and changes in (c) MLD and (f) sea-ice concentration between the two configurations. The MLD and sea-ice concentration plots in Fig. 13 here differ from those in Figures 5 and 9, in that Figures 5 and 9 show (a,b) biases with respect to observations and (c) the change in biases with respect to observations, while Fig. 13 shows just (a,b,d,e) total MLD and sea-ice concentration and (c,f) the differences in total MLD and sea-ice concentration between the v2 and v2.1

configurations. Thus, pattern and maximum differences in Figs. 5(c), 9(c), and Fig. 13(c,f) are not expected to be in exact
245 agreement with each other.

While v2.1 showed slightly shallower MLDs than v2, both globally and in the subpolar gyre (outlined in the previous
section), different patterns emerge in the Nordic Seas (Fig. 13 a-c). In particular, we see a substantial deepening of the MLD
by several hundred meters south of Svalbard and the Fram Strait in v2.1 compared with v2. A similar global shoaling and
localized Nordic Seas deepening of the mixed layer was seen in both the Nucleus for European Modelling of the Ocean
250 (NEMO) model (Calvert et al., 2020) and several coupled Earth system models in Fox-Kemper et al. (2011). Due to the
emergence of this behavior only in fully coupled models and not in ocean-only models driven by normal year forcing, Fox-
Kemper et al. (2011) attributed this response to air-sea and ice-sea feedback triggered by the MLE parameterization. In E3SM,
while northern hemisphere sea ice concentration is still too large in both model configurations, it was less so in v2.1 (Fig. 9
and 13 d-e), resulting in a climatologically more open ocean in the Nordic Seas. Along with increased vertical mixing and
255 surface fluxes within that same region (not shown), we speculate that similar air-sea and ice-sea feedbacks triggered by the
MLE parameterization are leading to the greater Nordic Seas MLDs in v2.1.
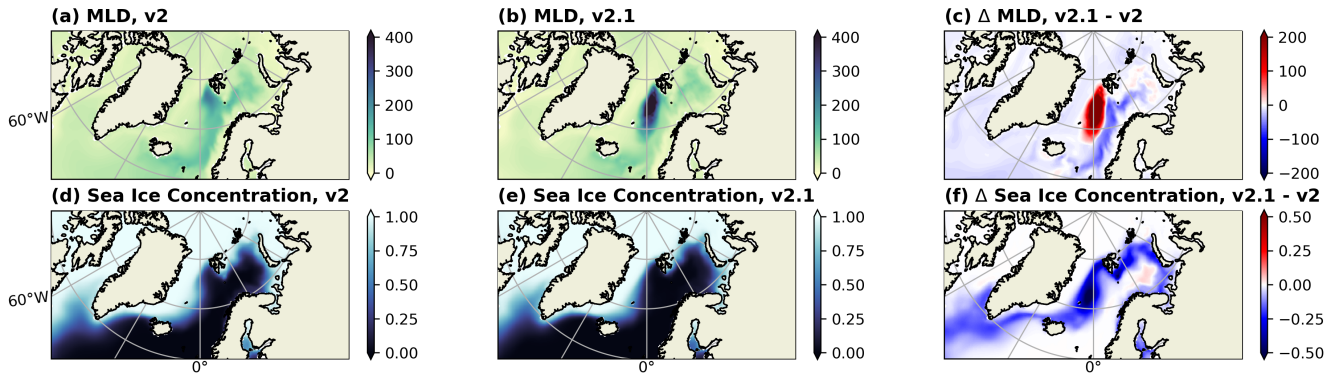
Figure 13. Annual climatological (a-b) MLD (m) and (d-e) sea-ice concentration (fraction) in the Nordic Seas for the (a,d) v2 and (b,e) v2.1
configurations. Change in (c) MLD and (f) sea-ice concentration between the v2.1 and v2 configurations.

To further understand the effects of these feedbacks and deeper MLDs, we examined several passive tracers. Figure 14 shows the North Atlantic passive tracer (a-d) concentration for the v2.1 configuration at various depths and (e-h) the change in concentration between the v2.1 and v2 configurations at those same depths. Most notably, panels (d) and (h) show tracer concentrations at depths greater than 1000m within the Nordic Seas and along the edge of the Nansen Basin are much higher in the v2.1 configuration than the v2 configuration. Combined with enhanced MLDs and mixing and reduced sea-ice coverage in Nordic Seas, the v2.1 configuration appears to form significantly more deep, dense water in this region that is then exported into the Arctic. By forming more deep water here that is exported to depth by vertical mixing, the cold, fresh biases present at the surface in v2 are reduced in v2.1.
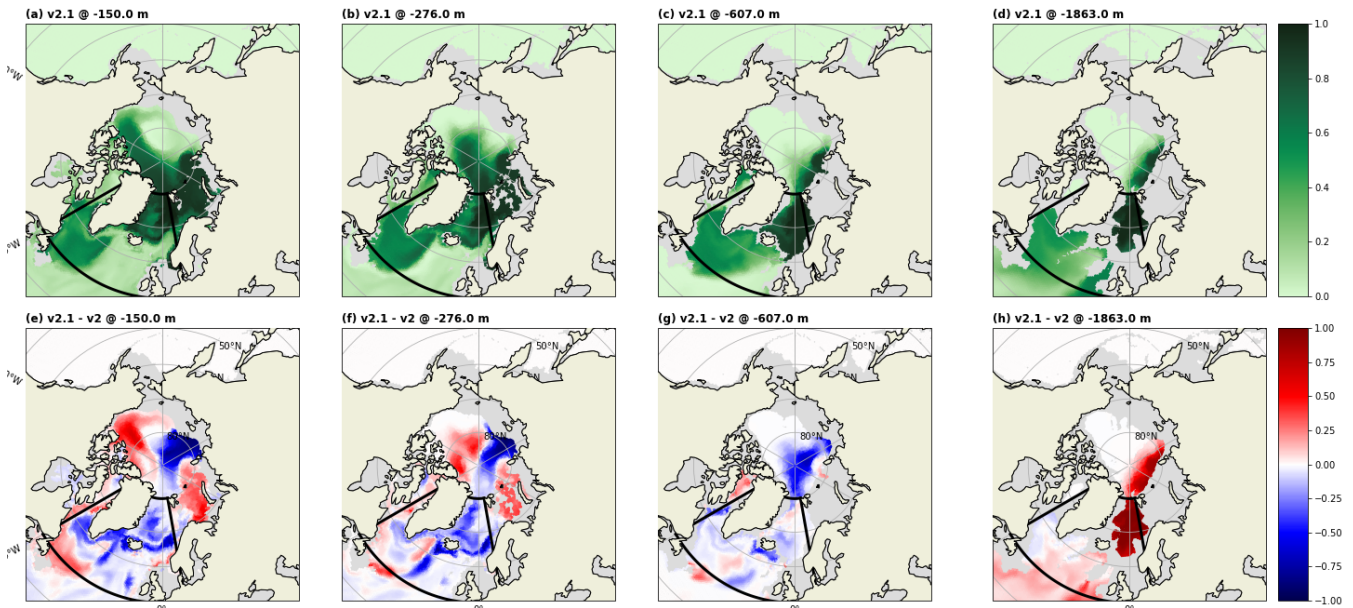
Figure 14. (a-d) Tracer concentration in the v2.1 configuration and (e-h) the change in concentration between the v2.1 and v2 configurations 33 years after tracer initiation at depths of (a,e) -150m, (b,f) -276m, (c,g) -607m, and (d,h) -1863m. Thick black boxes indicate the extent of the tracer surface forcing and light gray shading denotes bottom topography at that model depth.

265   However, the vast majority of this extra deep water is exported to the Arctic via North Atlantic Current flow through the Fram Strait (∼80% of the released tracer is north of 75°N at the end of the 33 years in both v2 and v2.1). Very little ends up below 1000m in the Atlantic, resulting in little change in the overturning circulation and providing a potential explanation for the lack of notable increase in the AMOC strength from v2 to v2.1. Figures 15 and 16 show changes in the winter and summer temperature and salinity along transects within the Labrador and Nordic Seas between the v2 and v2.1 configurations. Within

270   the Labrador Sea, where deep water is typically formed to feed the AMOC, we see very little change in the density/stratification structure between v2 and v2.1. A strong stratification buffer remains near the surface, preventing export of the cold, fresh water that remains there. Conversely, within the Nordic Seas, we see most of the interior stratification (below 1000m) has been eroded away by the full-depth mixing associated with the deeper MLDs there. This full-depth mixing is present for most of the 500 year *v2.1 piControl* simulation and appears to have developed very early on in both the Greenland and Norwegian Seas (see

275   Figure A4 in Appendix A). This lack of interior stratification and full-depth mixing allows for a greater connection of the surface to the deep, leading to greater export.
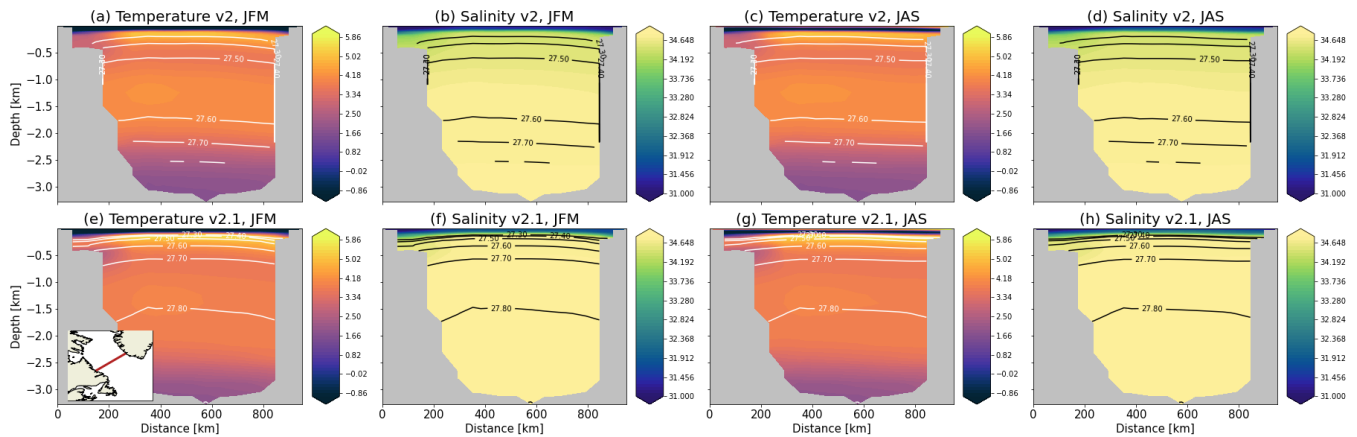
Figure 15. Annual climatological (a,c,e,g) temperature and (b,d,f,h) salinity in the (a,b,e,f) winter [JFM] and (c,d,g,h) summer [JAS] for the v2 (top row) and v2.1 (bottom row) configurations across a Labrador Sea transect (transect location shown in panel (e) inset). Black contour lines show select values of constant potential density.
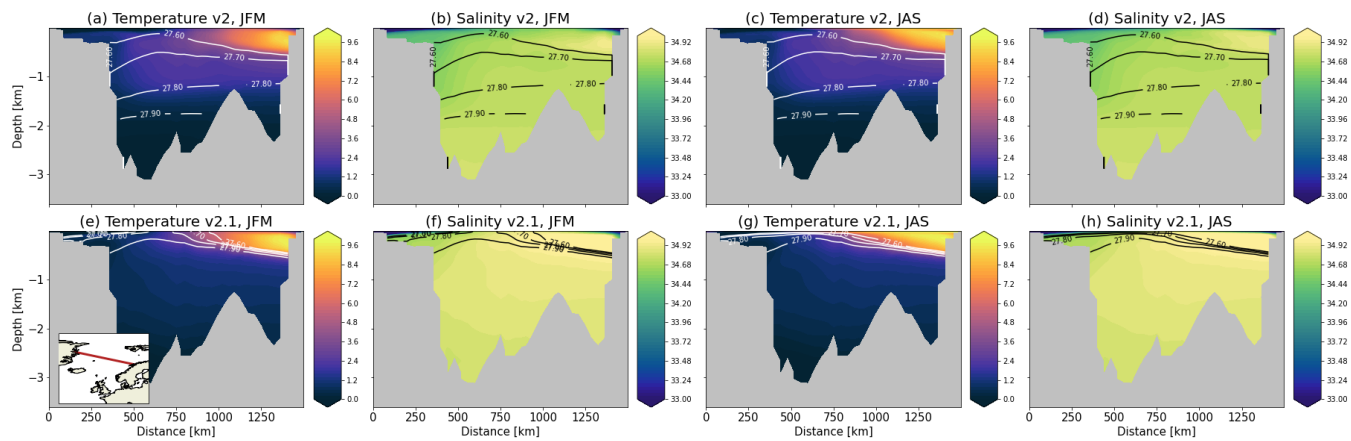
Figure 16. Same as Figure 15 but for a Nordic Seas transect.

Figure 17 further examines the formation of this deep water, by showing the surface water mass transformation in the North Atlantic basins for v2 (dotted line) and v2.1 (solid) over the *v2/v2.1 piControl Ext* runs. Surface water mass transformation diagnosed from surface heat and freshwater fluxes has been shown to vary with overturning strength in previous model com-

280 parison studies (Jackson and Petit, 2023; Petit et al., 2023). Here we diagnose surface water mass transformation by calculating surface buoyancy flux, excluding frazil ice formation, and area-integrating over defined regions following Speer and Tziperman (1992). The diagnosed surface water mass transformation highlights a clear difference with the added MLE parameterization. In most regions of the North Atlantic and Nordic Seas, introducing the MLE parameterization in v2.1 leads to the formation of denser waters, either from an increase in the density of the waters formed (a shift to the right in Fig. 17) and/or from an

285 increase in the water mass formation rate (visible as an increase in the peak value of the transformation rate). Specifically, in the v2.1 configuration, the North Atlantic Ocean shows a transformation rate peak (18.2 Sv) similar in magnitude to that of v2 (18.4 Sv), but shifted to higher densities: the range of dense water formed (visible as a negative slope in transformation) is 26 - 27.2 kg m^{-3} instead of the lighter 25.6 - 27 kg m^{-3} range of formation in the v2 configuration. Similarly, the dense water formation in the Norwegian Sea is shifted from 27.1 - 27.7 kg m^{-3} to 27.4 - 28 kg m^{-3} with the addition of the MLE

290 parameterization (with its magnitude remaining at approximately 4 Sv across both configurations). In other regions such as the Iceland Basin and Greenland Sea, both the peak transformation rate and the density range have increased in v2.1. In the Iceland Basin, the surface fluxes now form 2.4 Sv of dense water (27.2 - 27.6 kg m^{-3}) instead of the weaker 1.5 Sv of slightly lighter waters (27 - 27.4 kg m^{-3}) in v2. In the Greenland Sea, they form 1.4 Sv of dense water (27.9 - 28 kg m^{-3}) compared to the 0.8 Sv of lighter waters (27.6 - 27.8 kg m^{-3}) formed in v2 – a near doubling of dense water formation in that region.

295 In the Labrador and Irminger Seas, the transformation rates and changes to transformation are small compared to the regions mentioned above. It is important to note that these last two regions are considered important sites of convection and dense water mass formation in observations: convection in the Labrador Sea leads to important subpolar mode water formation, while deep water formation in the Irminger Sea is considered a major contributor to Atlantic Deep Water, AMOC (Petit et al., 2020), and possibly Labrador Sea Water (Pickart et al., 2003). Representing dense water formation in climate models in the correct

300 locations and appropriate magnitudes is an ongoing challenge, given that small-scale physical processes that contribute to it (e.g. convection, eddy mixing) are parameterized in models.
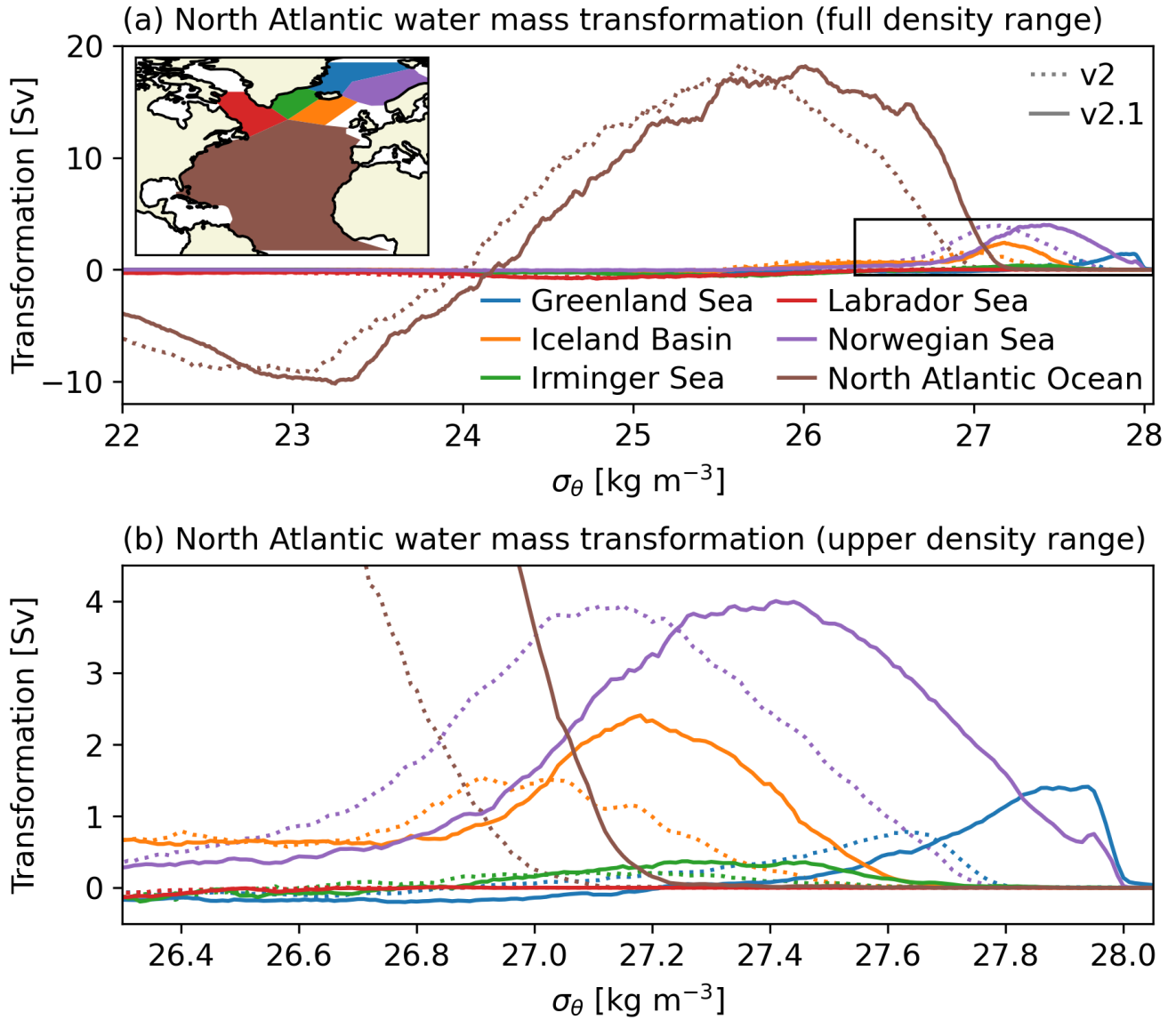
Figure 17. Surface water mass transformation in select North Atlantic basins in the v2.1 (solid) and v2 (dotted lines) configurations averaged over the 33-year *piControl Ext* runs (years 501-533). Panel (a) shows the full analyzed density range, while panel (b) zooms in on the higher density classes relevant to the subpolar basins shown. The extent of each region is shown in the map inset in panel (a). The x-axis σ_θ is the surface-referenced potential density minus 1000 kg m^{-3}. Transformation is calculated over a 0.01 kg m^{-3} density bin width, with a boxcar filter applied over a 5-bin smoothing window to reduce noise.

5 Conclusions

Overall, the v2.1 configuration resulted in some improvements to North Atlantic ocean biases, particularly SST and SSS (Figures 3 and 4), which resulted in improved sea-ice concentration in the North Atlantic (Figure 9). Changes to MLD biases were as expected, mirroring FK11 with a general shoaling of the mixed layer (Fox-Kemper et al., 2011) visible in many regions (Figure 5), though coupled feedbacks lead to regional deepening of the MLD that reduced the mean MLD bias globally (Figure 1). Additionally, though MLD is underestimated in comparison to observations in most regions, it does not appear to lead to any widespread degradation in the climate.

AMOC magnitude increased slightly with the addition of the MLE parameterization (Figure 6). This may be expected, since the direct effect of the FK11 parameterization on AMOC appears to be model-dependent and tends to either stabilize or minimally affect AMOC (Fox-Kemper et al., 2011). This effect holds for the v2.1 ensemble of simulations, which showed less variability in AMOC overall. Differences in AMOC may be due at least in part to a relocation of the site of deep convection from the Labrador and Irminger Seas and North Atlantic to the Nordic Seas (Fox-Kemper et al., 2011). This hypothesis aligns with changes we saw to our modeled MLDs in v2.1 when compared with v2.

There appear to be differences in MLD in the Nordic Seas that are separate from the overall MLD shoaling created in v2.1, indicating potential changes in deep water formation there (Figure 13). Similar to Fox-Kemper et al. (2011), we also saw deep convection occurring in the Nordic Seas rather than in the Labrador and Irminger Seas. Our water mass transformation analysis shows changes in deep water formation, particularly in the North Atlantic and Norwegian Sea, with more dense water being formed in v2.1 than in v2 (Figure 17). While it's not clear why this is the case, it does explain why our modeled AMOC improves slightly while not drastically altering the North Atlantic Subpolar Gyre. If increased deep water formation was occurring in the Labrador and Irminger Seas, we would expect to see a great decrease in the SSS, SST, and sea-ice biases there. The passive tracer transport analysis in Section 4 for v2.1 indicates that the increased deep convection may not translate to a better AMOC because the dense water formed is transported northward into the Arctic, rather than towards the south. Comparison of tracer advection from v2 to v2.1 shows deep northward convection from the Barents Sea into the Arctic in v2.1; this does not occur in v2. Future work will attempt to elucidate mechanisms behind this shift in deep water formation.

Our results also indicate that the climatological characteristics of many surface and atmospheric fields in E3SMv2.1 have improved compared to v2 (Figure 7). We have also examined the model performance of seven inter-annual extratropical modes of variability, including the atmospheric-based NAM, NAO, PNA, NPO, and SAM, as well as two modes based on sea-surface temperature (SST): the PDO, and NPGO. Our results suggest noticeable improvement in the NAO and NAM, however, for most modes and seasons we find the large-scale extratropical modes of variability in E3SMv2.1 are not significantly different from v2 (Figure 8). Orbe et al. (2020) distinguished two classes of model improvement: (1) "those that rely on a threshold of model representation that is crossed at a distinct moment in model development", and (2) "improvements that rely on more gradual, collective improvements in processes." They argue that the performance evolution of extratropical modes of variability likely fall into the second category, e.g., due to enhancements in base climate representation and relevant processes, which might be evidenced via mixed influences across different modes and seasons. Additionally, the sample size available for this study

limits any robust conclusions regarding performance changes in the simulation of extratropical modes of variability. Lastly, our analysis indicates that the TCR and ECS are essentially unchanged in E3SMv2.1 compared to v2.

Code and data availability. The E3SM code is available at https://github.com/E3SM-Project/E3SM, and the model versions used for the simulations presented here are E3SM v2.1 (DOI: 10.5281/zenodo.7527568) and v2 (DOI: 10.5281/zenodo.5563151). A full list of all
340 code changes made from v2 to v2.1 can be found here: https://github.com/E3SM-Project/E3SM/pulls?q=is%3Apr+is%3Aclosed+merged%3A2021-10-11..2023-01-11+base%3Amaster. Information about running the model is available at https://e3sm.org/model/running-e3sm. The simulation data used for this paper is published to CMIP6 through the Earth System Grid Federation (ESGF). Data is available from https://esgf-node.cels.anl.gov/search/cmip6/ under source_id=E3SM-2-1. Preliminary analysis on the ocean component MPAS-Ocean was performed using MPAS-Analysis, available at https://github.com/MPAS-Dev/MPAS-Analysis (doi 10.5281/zenodo.4407459).

345 **Appendix A: Supplementary Figures**
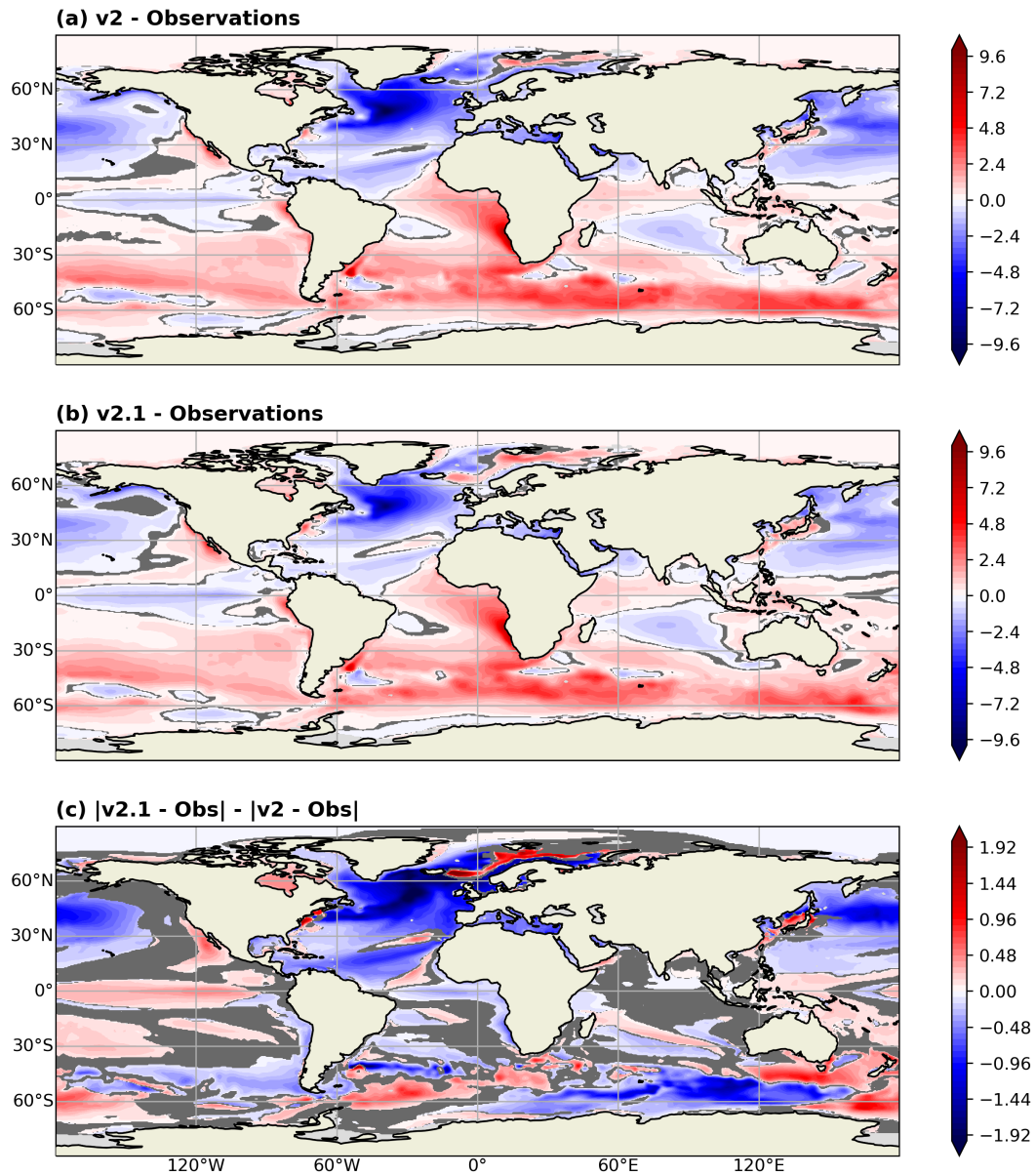
Figure A1. Global annual climatological SST biases (°C) with respect to observations for the (a) v2 and (b) v2.1 configurations. (c) Change in SST biases between v2.1 and v2 configurations. Regions shaded in light gray denote where there is no data and regions shaded in dark gray denote where the difference is not significant (according to a one-sample T-test in (a),(b) and a two-sample T-test in (c)).
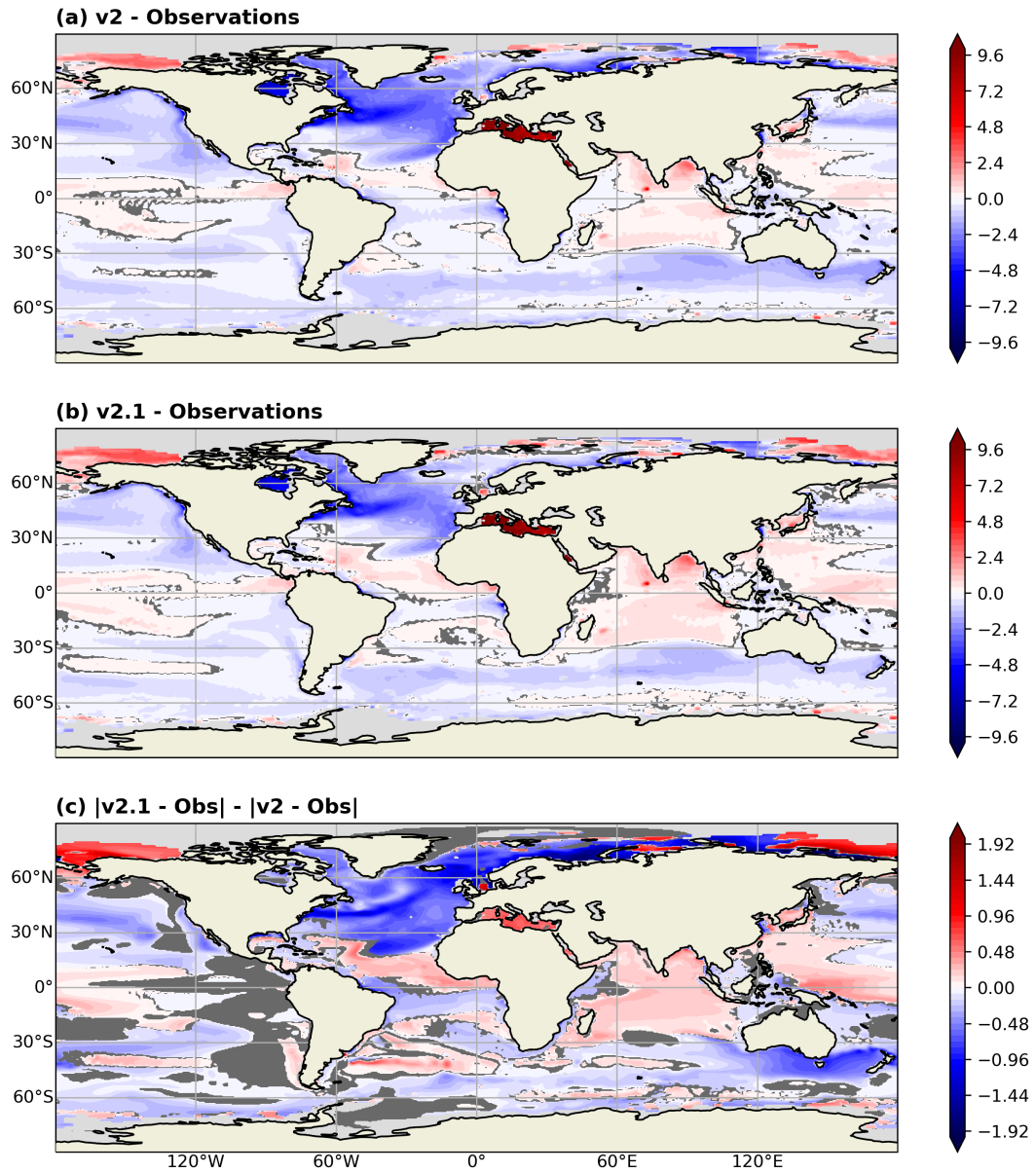
Figure A2. Same as Figure A1 but for SSS (psu).
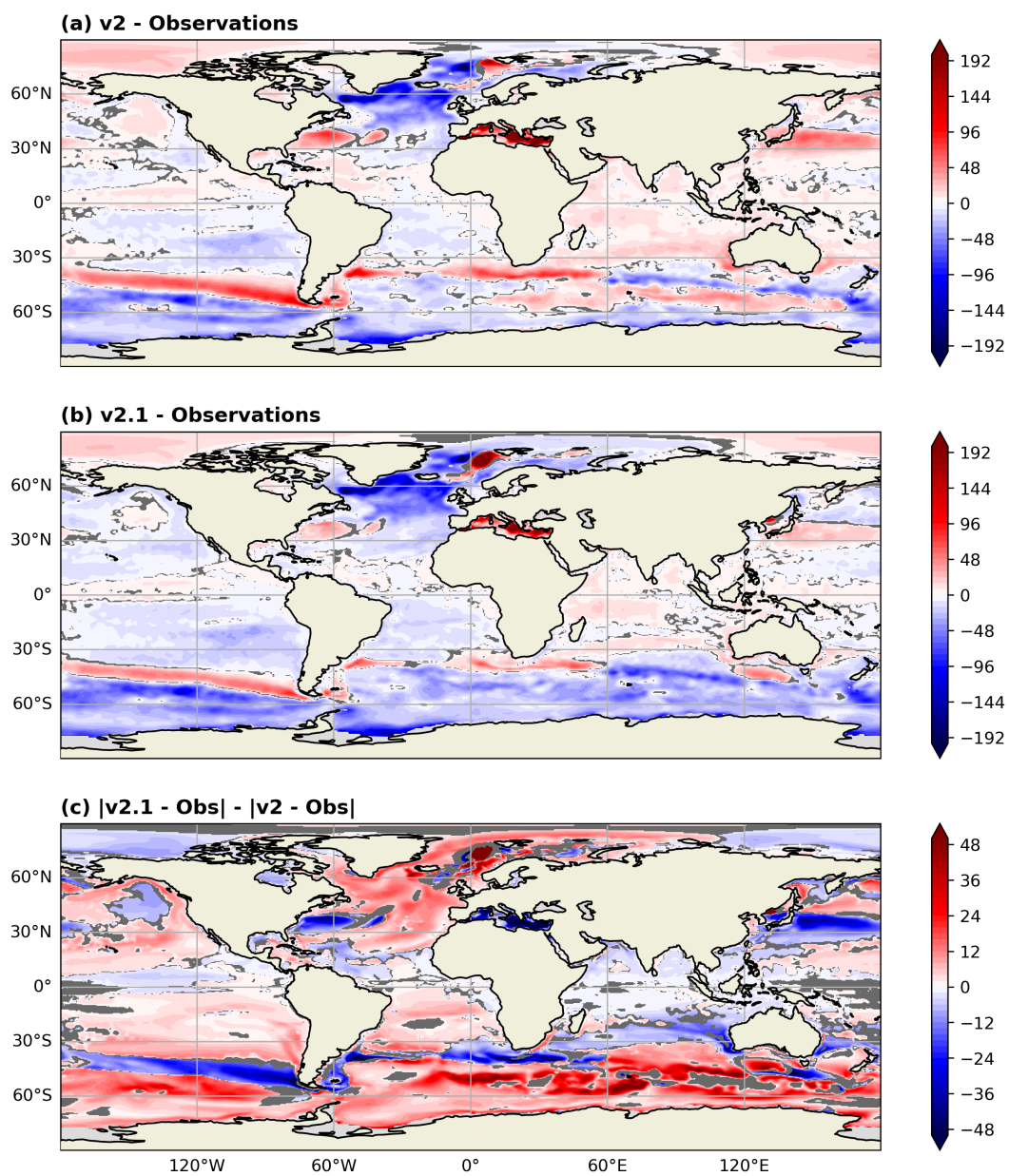
Figure A3. Same as Figure A1 but for MLD (m).
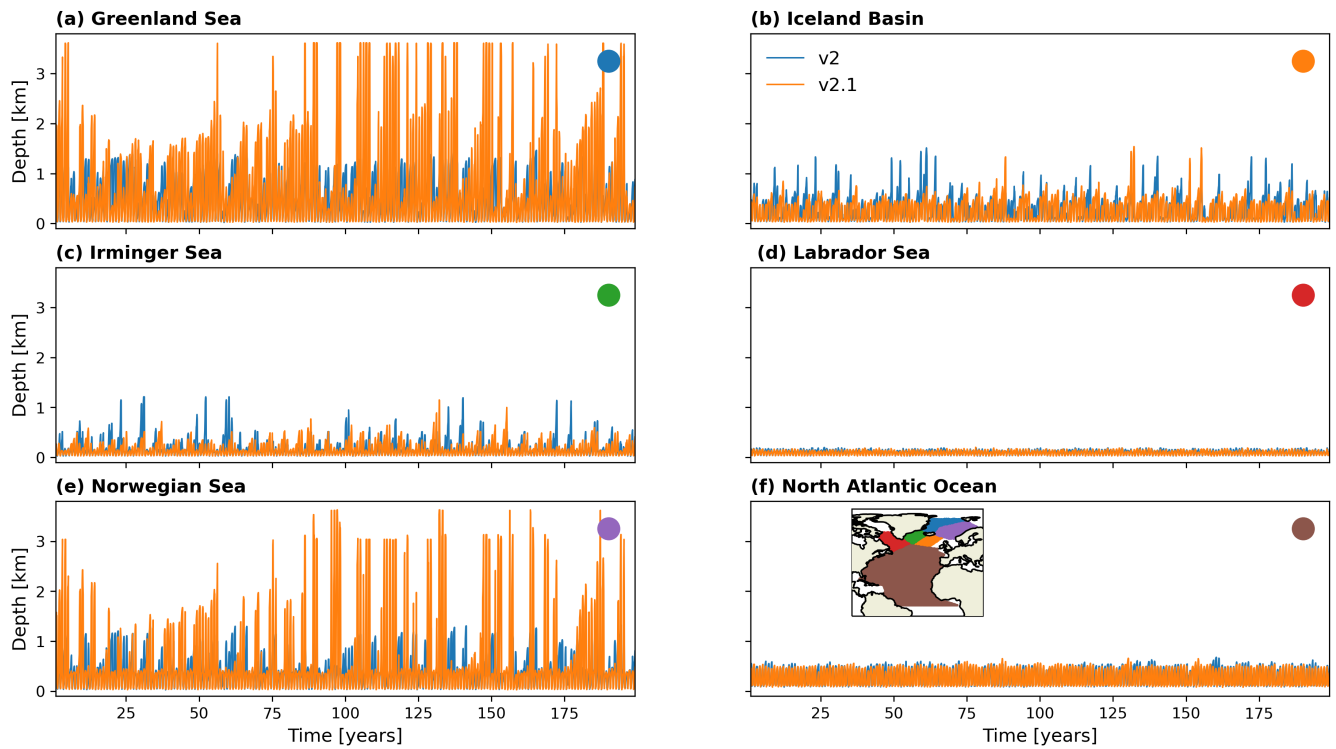
Figure A4. Maximum mixed layer depth (m) for the first 200 years of the *v2 piControl* (blue lines) and *v2.1 piControl* (orange lines) in the North Atlantic basins: the (a) Greenland Sea, (b) Iceland Basin, (c) Irminger Sea, (d) Labrador Sea, (e) Norwegian Sea, and (f) North Atlantic Ocean. Scope of each region is shown in the map inset in panel (f) and correspond to the same regions used in Figure 17.
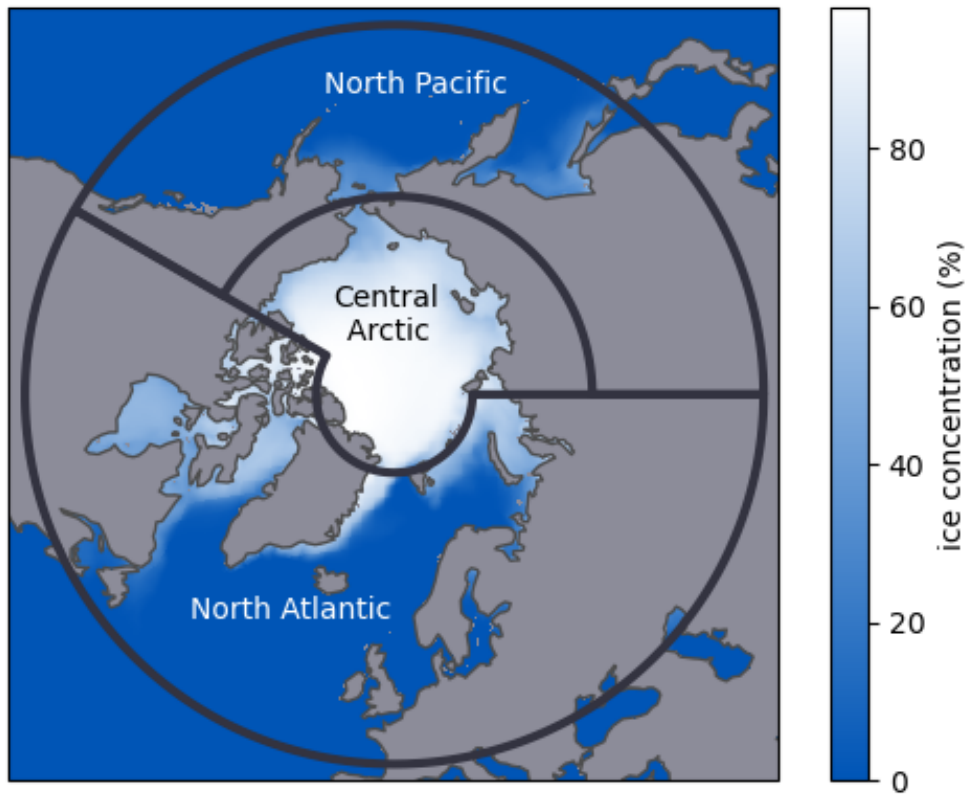
Figure A5. Partitioned Arctic geographical regions for the sea-ice area analysis in Section 3.4 Figures 11 and 12 (Ivanova et al., 2016).
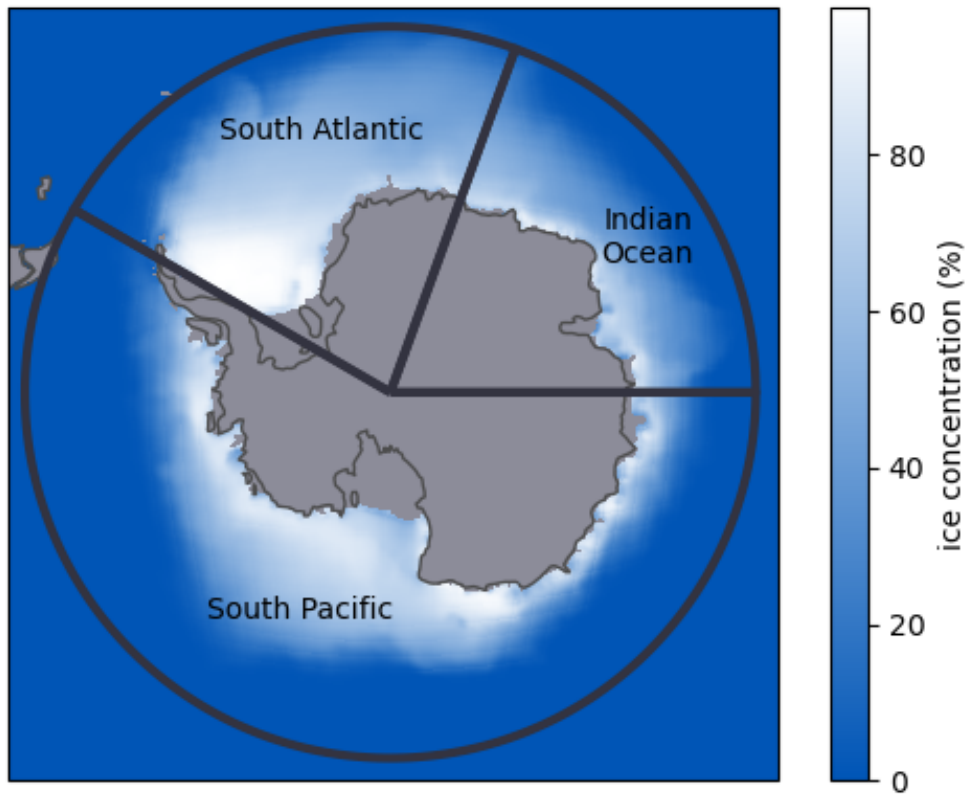
Figure A6. Same as Figure A5 but for the Antarctic.

Appendix B: Code Changes from v2 to v2.1

B1 Atmosphere

The atmosphere component of E3SM remains the E3SM Atmosphere Model (EAM). While there were no major changes in the default configuration of EAM from version 2, several new stealth features are included in the base code, but were not active in the simulations analyzed in this study: a semi-Lagrangian tracer transport for theta-l dycore; a new algorithm for finding the tropopause; and new regionally refined mesh configurations.

B2 Ocean

The ocean component of E3SM remains MPAS-Oean. Beyond the FK11 MLE parameterization discussed in detail in the main part of this manuscript, a correction for barotropic thickness consistency that reduces divergence noise and the addition of an ocean carbon conservation analysis member were made.

B3 Sea Ice

The sea ice component of E3SM remains MPAS-Seaice. From v2 to v2.1 a correction to how shortwave parameters are interpolated in the SNICAR-AD 5-band radiation scheme, the addition of a sea ice carbon conservation analysis member, updates to the default sea ice biogeochemistry namelist parameters to be consistent with v2 improvements to nitrogen cycling, and a correction in the ice-ocean dissolved organic nitrogen coupling were made.

B4 Land

The land component of E3SM remains the E3SM Land Model (ELM). While there were no major changes in the default configuration of ELM, several optional stealth features have been added in the base code, but were not active in the simulations analyzed in this study: an implementation of topography-based subgrid structure and accompanying parameterizations and atmospheric forcing downscaling; a new plant hydrolics scheme; two-way land-river hydrological coupling through the infiltration of floodplain water; an implementation of perennial crops; updates to the SNICAR-AD snow radiative transfer model; and an implementation of soil erosion and sediment yield in ELM-Erosion.

B5 River

The river component of E3SM remains the Model for Scale Adaptive River Transport (MOSART). While there were no major changes in the default configuration of MOSART, an optional stealth feature of two-way river-ocean hydrological coupling between MOSART and MPAS-Ocean was added to the base code, but was not active in the simulations analyzed in this study.

B6 Coupled System

The coupler in E3SM remains cpl7 Craig et al. (2012). Small bug fixes in the land-atmosphere fluxes and in the zenith angle calculation were made, along with the option to calculate carbon budgets when heat and water budgets are active.

375 *Author contributions.* KS, AB, LC, LVR, CB, MP, KB, OG, JW, MM, WL, and AH contributed to the improvements of AMOC and bias representation in E3SM. PG, JL, AO, and CZ are model evaluation contributors to the PCMDI Metrics Package, and PG, JL, and AO provided the atmosphere and part of the sea-ice analysis and text. JCG and LVR ran the v2.1 simulation campaign. CB, JB, GB, YF, JCG, WH, BH, NJ, WL, PM, MM, MP, BS, QT, TT, JW, SX, XZ contributed to the v2.1 model development and analysis. CZ and TB contributed to the post-processing, quality control, and publishing of the data to ESGF. JB, BM, and AB contributed to the WMT analysis and text. KS took
380 the lead in writing the manuscript, with significant contributions from AB, LC, JL, AO, and PG. All authors provided critical feedback and helped shape the research, analysis, and manuscript.

Competing interests. One of the co-authors is a member of the editorial board of Geoscientific Model Development.

Acknowledgements. This work was supported in part by the Biological and Environmental Research program as part of the Earth System Model Development (ESMD) program area's E3SM project, funded by the US Department of Energy (DOE), Office of Science. This research
385 used a high-performance computing cluster provided by the BER Earth System Modeling program and operated by the Laboratory Computing Resource Center at Argonne National Laboratory. This research also used resources of the National Energy Research Scientific Computing Center, a DOE Office of Science User Facility supported by the Office of Science of the U.S. Department of Energy under Contract No. DE-AC02-05CH11231. This work was also partially supported by the Regional and Global Model Analysis (RGMA) component of the Earth and Environmental System Modeling Program of the U.S. Department of Energy's Office of Science BER program via National
390 Science Foundation (NSF) IA 1947282 (DE-SC0022070). Los Alamos National Laboratory is operated by Triad National Security, LLC for the U.S. Department of Energy, National Nuclear Security Administration under Contract 89233218CNA000001. Lawrence Livermore National Laboratory is operated by Lawrence Livermore National Security, LLC, for the U.S. Department of Energy, National Nuclear Security Administration under Contract DE-AC52-07NA27344. The Pacific Northwest National Laboratory is operated by Battelle for the DOE under Contract DE-AC05-76RL01830. The National Center for Atmospheric Research is sponsored by the NSF of the United States of
395 America under Cooperative Agreement No. 1852977. This paper describes objective technical results and analysis. Any subjective views or opinions that might be expressed in the paper do not necessarily represent the views of the U.S. Department of Energy or the United States Government.

References

Adcroft, A. and Hallberg, R.: On methods for solving the oceanic equations of motion in generalized vertical coordinates, Ocean Modelling, 11, 224–233, 2006.

Adcroft, A. J., Anderson, W., Blanton, C., Bushuk, M., Dufour, C. O., Dunne, J. P., Griffies, S. M., Hallberg, R. W., Harrison, M. J., Held, I., Jansen, M., John, J., Krasting, J. P., Langenhorst, A., Legg, S., Liang, Z., McHugh, C., Reichl, B. G., Radhakrishnan, A., Rosati, T., Samuels, B., Shao, A., Stouffer, R. J., Winton, M., Wittenberg, A. T., Xiang, B., Zadeh, N., and Zhang, R.: The GFDL global ocean and sea ice model OM4.0: Model description and simulation features., Journal of Advances in Modeling the Earth System, 11, 2019.

Boccaletti, G., Ferrari, R., and Fox-Kemper, B.: Mixed Layer Instabilities and Restratification, Journal of Physical Oceanography, 37, 2228––2250, https://doi.org/10.1175/JPO3101.1, 2007.

Bodner, A. S., Fox-Kemper, B., Johnson, L., Roekel, L. P. V., McWilliams, J. C., Sullivan, P. P., Hall, P. S., and Dong, J.: Modifying the Mixed Layer Eddy Parameterization to Include Frontogenesis Arrest by Boundary Layer Turbulence, Journal of Physical Oceanography, 53, 2023.

Boyer, T. P., Baranova, O. K., Coleman, C., Garcia, H. E., Grodsky, A., Locarnini, R. A., Mishonov, A. V., Paver, C. R., Reagan, J. R., Seidov, D., Smolyar, I. V., Weathers, K. W., and Zweng, M. M.: World Ocean Database 2018, NOAA Atlas NESDIS 87. v2020.2, National Centers for Environmental Information Ocean Climate Laboratory, 2018.

Burrows, S. M., Maltrud, M., Yang, X., Zhu, Q., Jeffery, N., Shi, X., Ricciuto, D., Wang, S., Bisht, G., Tang, J., Wolfe, J., Harrop, B. E., Singh, B., Brent, L., Baldwin, S., Zhou, T., Cameron-Smith, P., Keen, N., Collier, N., Xu, M., Hunke, E. C., Elliott, S. M., Turner, A. K., Li, H., Wang, H., Golaz, J.-C., Bond-Lamberty, B., Hoffman, F. M., Riley, W. J., Thornton, P. E., Calvin, K., and Leung, L. R.: The DOE E3SM v1.1 Biogeochemistry Configuration: Description and Simulated Ecosystem-Climate Responses to Historical Changes in Forcing, Journal of Advances in Modeling Earth Systems, 12, https://doi.org/10.1029/2019ms001766, 2020.

Caldwell, P. M., Mametjanov, A., Tang, Q., Van Roekel, L. P., Golaz, J. C., Lin, W., Bader, D. C., Keen, N. D., Feng, Y., Jacob, R., Maltrud, M. E., Roberts, A. F., Taylor, M. A., Veneziani, M., Wang, H., Wolfe, J. D., Balaguru, K., Cameron-Smith, P., Dong, L., Klein, S. A., Leung, L. R., Li, H. Y., Li, Q., Liu, X., Neale, R. B., Pinheiro, M., Qian, Y., Ullrich, P. A., Xie, S., Yang, Y., Zhang, Y., Zhang, K., and Zhou, T.: The DOE E3SM Coupled Model Version 1: Description and Results at High Resolution, Journal of Advances in Modeling Earth Systems, 11, 4095–4146, https://doi.org/10.1029/2019MS001870, 2019.

Calvert, D., Nurser, G., Bell, M. J., and Fox-Kemper, B.: The impact of a parameterisation of submesoscale mixed layer eddies on mixed layer depths in the NEMO ocean model, Ocean Modelling, 154, 2020.

Comeau, D., Asay-Davis, X. S., Begeman, C. B., Hoffman, M. J., Lin, W., Petersen, M. R., Price, S. F., Roberts, A. F., Roekel, L. P. V., Veneziani, M., Wolfe, J. D., Fyke, J. G., Ringler, T. D., and Turner, A. K.: The DOE E3SM v1.2 Cryosphere Configuration: Description and Simulated Antarctic Ice-Shelf Basal Melting, Journal of Advances in Modeling Earth Systems, 14, https://doi.org/10.1029/2021ms002468, 2022.

Comiso, J. C.: Bootstrap Sea Ice Concentrations from Nimbus-7 SMMR and DMSP SSM/I-SSMIS, Version 3, https://doi.org/10.5067/7Q8HCCWS4I0R, 2017.

Craig, A. P., Vertenstein, M., and Jacob, R.: A new flexible coupler for earth system modeling developed for CCSM4 and CESM1, The International Journal of High Performance Computing Applications, 26, 2012.

Danabasoglu, G., Lamarque, J.-F., Bacmeister, J., Bailey, D. A., DuVivier, A. K., Edwards, J., Emmons, L. K., Fasullo, J., Garcia, R., Gettelman, A., Hannay, C., Holland, M. M., Large, W. G., Lauritzen, P. H., Lawrence, D. M., Lenaerts, J. T. M., Lindsay, K., Lipscomb,

435   W. H., Mills, M. J., Neale, R., Oleson, K. W., Otto-Bliesner, B., Phillips, A. S., Sacks, W., Tilmes, S., Kampenhout, L., Vertenstein, M.,
       Bertini, A., Dennis, J. M., Deser, C., Fischer, C., Fox-Kemper, B., Kay, J. E., Kinnison, D., Kushner, P. J., Larson, V. E., Long, M. C.,
       Mickelson, S., Moore, J. K., Nienhouse, E., Polvani, L., Rasch, P. J., and Strand, W. G.: The Community Earth System Model Version 2
       (CESM2), Journal of Advances in Modeling Earth Systems, 12, https://doi.org/10.1029/2019ms001916, 2020.

       de Boyer Montégut, C., Madec, G., Fischer, A. S., Lazar, A., and Iudicone, D.: Mixed layer depth over the global ocean: An examination of
440   profile data and a profile-based climatology, Journal of Geophysical Research: Oceans, 109, 2004.

       Eyring, V., Bony, S., Meehl, G. A., Senior, C. A., Stevens, B., Stouffer, R. J., and Taylor, K. E.: Overview of the Coupled Model
       Intercomparison Project Phase 6 (CMIP6) experimental design and organization, Geoscientific Model Development, 9, 1937–1958,
       https://doi.org/10.5194/gmd-9-1937-2016, 2016.

       Fox-Kemper, B., Ferrari, R., and Hallberg, R.: Parameterization of Mixed Layer Eddies. Part I: Theory and Diagnosis, Journal of Physical
445   Oceanography, 38, 1145–1165, https://doi.org/10.1175/2007JPO3792.1, 2008.

       Fox-Kemper, B., Danabasoglu, G., Ferrari, R., Griffies, S., Hallberg, R., Holland, M., Maltrud, M., Peacock, S., and Samuels, B.: Parameter-
       ization of mixed layer eddies. III: Implementation and impact in global ocean climate simulations, Ocean Modeling, 39, 61–78, 2011.

       Gent, P. R. and Mcwilliams, J. C.: Isopycnal Mixing in Ocean Circulation Models, Journal of Physical Oceanography, 20, 150–155,
       https://doi.org/10.1175/1520-0485(1990)020<0150:IMIOCM>2.0.CO;2, 1990.

450   Gleckler, P. J., Taylor, K. E., and Doutriaux, C.: Performance metrics for climate models, Journal of Geophysical Research, 113, 2008.

       Golaz, J.-C., Caldwell, P. M., Van Roekel, L. P., Petersen, M. R., Tang, Q., Wolfe, J. D., Abeshu, G., Anantharaj, V., Asay-Davis, X. S.,
       Bader, D. C., Baldwin, S. A., Bisht, G., Bogenschutz, P. A., Branstetter, M., Brunke, M. A., Brus, S. R., Burrows, S. M., Cameron-Smith,
       P. J., Donahue, A. S., Deakin, M., Easter, R. C., Evans, K. J., Feng, Y., Flanner, M., Foucar, J. G., Fyke, J. G., Griffin, B. M., Hannay, C.,
       Harrop, B. E., Hoffman, M. J., Hunke, E. C., Jacob, R. L., Jacobsen, D. W., Jeffery, N., Jones, P. W., Keen, N. D., Klein, S. A., Larson,
455   V. E., Leung, L. R., Li, H.-Y., Lin, W., Lipscomb, W. H., Ma, P.-L., Mahajan, S., Maltrud, M. E., Mametjanov, A., McClean, J. L., McCoy,
       R. B., Neale, R. B., Price, S. F., Qian, Y., Rasch, P. J., Reeves Eyre, J. E. J., Riley, W. J., Ringler, T. D., Roberts, A. F., Roesler, E. L.,
       Salinger, A. G., Shaheen, Z., Shi, X., Singh, B., Tang, J., Taylor, M. A., Thornton, P. E., Turner, A. K., Veneziani, M., Wan, H., Wang, H.,
       Wang, S., Williams, D. N., Wolfram, P. J., Worley, P. H., Xie, S., Yang, Y., Yoon, J.-H., Zelinka, M. D., Zender, C. S., Zeng, X., Zhang, C.,
       Zhang, K., Zhang, Y., Zheng, X., Zhou, T., and Zhu, Q.: The DOE E3SM Coupled Model Version 1: Overview and Evaluation at Standard
460   Resolution, Journal of Advances in Modeling Earth Systems, 11, 2089–2129, https://doi.org/10.1029/2018MS001603, 2019.

       Golaz, J.-C., Van Roekel, L. P., Zheng, X., Roberts, A., Wolfe, J. D., Lin, W., Bradley, A., Tang, Q., Maltrud, M. E., Forsyth, R. M., and
       et al.: The DOE E3SM Model Version 2: Overview of the physical model and initial model evaluation, Earth and Space Science Open
       Archive, p. 68, https://doi.org/10.1002/essoar.10511174.2, 2022.

       Gregory, J. M., Ingram, W. J., Palmer, M. A., Jones, G. S., Stott, P. A., Thorpe, R. B., Lowe, J. A., Johns, T. C., and Williams, K. D.: A new
465   method for diagnosing radiative forcing and climate sensitivity, Geophys. Res. Lett., 31, 2004.

       Griffies, S. M.: Elements of MOM4p1, Tech. rep., NOAA/Geophysical Fluid Dynamics Laboratory Ocean Group, 2009.

       Hurrell, J. W., Hack, J. J., Shea, D., Caron, J. M., and Rosinski, J.: A new sea surface temperature and sea ice boundary dataset for the
       Community Atmosphere Model, Journal of Climate, 21, 5145–5153, 2008.

       Hurrell, J. W., Holland, M. M., Gent, P. R., Ghan, S., Kay, J. E., Kushner, P. J., Lamarque, J.-F., Large, W. G., Lawrence, D., Lindsay, K.,
470   Lipscomb, W. H., Long, M. C., Mahowald, N., Marsh, D. R., Neale, R. B., Rasch, P., Vavrus, S., Vertenstein, M., Bader, D., Collins, W. D.,
       Hack, J. J., Kiehl, J., and Marshall, S.: The Community Earth System Model: A Framework for Collaborative Research, Bulletin of the
       American Meteorological Society, 94, 1339–1360, https://doi.org/10.1175/bams-d-12-00121.1, 2013.

Ivanova, D. P., Gleckler, P. J., Taylor, K. E., Durack, P. J., , and Marvel, K. D.: Moving beyond the Total Sea Ice Extent in Gauging Model Biases, Journal of Climate, 29, 8965–8987, 2016.

475 Jackson, L. C. and Petit, T.: North Atlantic overturning and water mass transformation in CMIP6 models, Clim. Dyn., 60, 2871–2891, https://doi.org/10.1007/s00382-022-06448-1, 2023.

Lagerloef, G., Kao, H., Meissner, T., and Vazquez, J.: Aquarius salinity validation analysis; data version 4.0, Earth Space Res., Seattle, WA, USA, 2015.

Laurindo, L. C., Mariano, A. J., and Lumpkin, R.: An improved near-surface velocity climatology for the global ocean from drifter observa-
480 tions, Deep Sea Research Part I: Oceanographic Research Papers, 124, 73–92, 2017.

Lee, J., Sperber, K. R., Gleckler, P. J., Bonfils, C., and Taylor, K. E.: Quantifying the agreement between observed and simulated extratropical modes of interannual variability, Climate Dynamics, 52, 4057–4089, 2019.

Lee, J., Sperber, K. R., Gleckler, P. J., Taylor, K. E., and Bonfils, C.: Benchmarking performance changes in the simulation of extratropical modes of variability across CMIP generations, Journal of Climate, 34, 6945–6969, 2021.

485 Lee, J., Gleckler, P. J., Ahn, M.-S., Ordonez, A., Ullrich, P., Sperber, K. R., Taylor, K. E., Planton, Y. Y., Guilyardi, E., Durack, P., Bonfils, C., Zelinka, M. D., Chao, L.-W., Dong, B., Doutriaux, C., Zhang, C., Vo, T., Boutte, J., Wehner, M. F., Pendergrass, A. G., Kim, D., Xue, Z., Wittenberg, A. T., and Krasting, J.: Systematic and Objective Evaluation of Earth System Models: PCMDI Metrics Package (PMP) version 3, Geoscientific Model Development, 17, 3919–3948, https://doi.org/10.5194/gmd-17-3919-2024, 2024.

Marshall, J., Adcroft, A., Hill, C., L. Perelman, L., , and Heisey, C.: A finite-volume, incompressible Navier Stokes model for studies of the
490 ocean on parallel computers, J. Geophysical Res., 102, 5753–5766, 1997.

Meehl, G. A., Senior, C. A., Eyring, V., Flato, G., Lamarque, J. F., Stouffer, J. R., Taylor, K. E., and Schlund, M.: Context for interpreting equilibrium climate sensitivity and transient climate response from the CMIP6 Earth system models, Science Advances, 6, 2020.

Ocean, E. and Facility, S. I. S. A.: EUMETSAT, 2022: OSI SAF Global sea ice concentration climate data record 1978-2020 (v3.0, 2022), Tech. rep., EUMETSAT, 2022.

495 Orbe, C., Roekel, L. V., Adames, A., Danabasoglu, G., Dezfuli, A., Fasullo, J., Gleckler, P., Lee, J., Li, W., Nazarenko, L., Schmidt, G., Sperber, K., and Zhao, M.: Representation of Modes of Variability in 6 U.S. Climate Models, Journal of Climate, 33, 7591–7617, https://doi.org/10.1175/JCLI-D-19-0956.1, 2020.

Petit, T., Lozier, M. S., Josey, S. A., and Cunningham, S. A.: Atlantic Deep Water Formation Occurs Primarily in the Iceland Basin and Irminger Sea by Local Buoyancy Forcing, Geophysical Research Letters, 47, e2020GL091 028, https://doi.org/10.1029/2020GL091028,
500 e2020GL091028 2020GL091028, 2020.

Petit, T., Robson, J., Ferreira, D., and Jackson, L. C.: Understanding the sensitivity of the North Atlantic subpolar Ooerturning in different resolution versions of HadGEM3-GC3.1, J. Geophys. Res. Oceans, 128, e2023JC019672, https://doi.org/10.1029/2023JC019672, 2023.

Pickart, R. S., Straneo, F., and Moore, G.: Is Labrador Sea Water formed in the Irminger basin?, Deep Sea Research Part I: Oceanographic Research Papers, 50, 23–52, https://doi.org/10.1016/S0967-0637(02)00134-6, 2003.

505 Redi, M.: Oceanic Isopycnal Mixing by Coordinate Rotation, Journal of Physical Oceanography, 12, 1154–1158, 1982.

Smith, R., Jones, P., Briegleb, B., Bryan, F., Danabasoglu, G., Dennis, J., Dukowicz, J., Eden, C., Fox-Kemper, B., Gent, P., Hecht, M., Jayne, S., Jochum, M., Large, W., Lindsay, K., Maltrud, M., Norton, N., Peacock, S., Vertenstein, M., and Yeager, S.: The Parallel Ocean Program (POP) Reference Manual, Environmental Science, Physics, pp. 1–140, 2010.

Speer, K. and Tziperman, E.: Rates of water mass formation in the north Atlantic Ocean, J. Phys. Oceanogr., 22, 93–104,
510 https://doi.org/10.1175/1520-0485(1992)022<0093:ROWMFI>2.0.CO;2, 1992.

Tang, Q., Golaz, J.-C., Van Roekel, L. P., Taylor, M. A., Lin, W., Hillman, B. R., Ullrich, P. A., Bradley, A. M., Guba, O., Wolfe, J. D., Zhou, T., Zhang, K., Zheng, X., Zhang, Y., Zhang, M., Wu, M., Wang, H., Tao, C., Singh, B., Rhoades, A. M., Qin, Y., Li, H.-Y., Feng, Y., Zhang, Y., Zhang, C., Zender, C. S., Xie, S., Roesler, E. L., Roberts, A. F., Mametjanov, A., Maltrud, M. E., Keen, N. D., Jacob, R. L., Jablonowski, C., Hughes, O. K., Forsyth, R. M., Di Vittorio, A. V., Caldwell, P. M., Bisht, G., McCoy, R. B., Leung, L. R., and Bader, D. C.: The fully coupled regionally refined model of E3SM version 2: overview of the atmosphere, land, and river results, Geoscientific Model Development, 16, 3953–3995, https://doi.org/10.5194/gmd-16-3953-2023, 2023.